An improved potential energy surface and multi-temperature quasiclassical trajectory calculations of $N_2 + N_2$ dissociation reactions

Jason D. Bender,[1] Paolo Valentini,[1] Ioannis Nompelis,[1] Yuliya Paukku,[2] Zoltan Varga,[2] Donald G. Truhlar,[2] Thomas Schwartzentruber,[1] and Graham V. Candler[1]
[1]*Department of Aerospace Engineering and Mechanics, University of Minnesota, Minneapolis, Minnesota 55455, USA*
[2]*Department of Chemistry, Chemical Theory Center, and Supercomputing Institute, University of Minnesota, Minneapolis, Minnesota 55455, USA*

(Received 19 February 2015; accepted 17 July 2015; published online 5 August 2015)

Accurate modeling of high-temperature hypersonic flows in the atmosphere requires consideration of collision-induced dissociation of molecular species and energy transfer between the translational and internal modes of the gas molecules. Here, we describe a study of the $N_2 + N_2 \longrightarrow N_2 + 2N$ and $N_2 + N_2 \longrightarrow 4N$ nitrogen dissociation reactions using the quasiclassical trajectory (QCT) method. The simulations used a new potential energy surface for the N_4 system; the surface is an improved version of one that was presented previously. In the QCT calculations, initial conditions were determined based on a two-temperature model that approximately separates the translational-rotational temperature from the vibrational temperature of the N_2 diatoms. Five values from 8000 K to 30 000 K were considered for each of the two temperatures. Over 2.4×10^9 trajectories were calculated. We present results for ensemble-averaged dissociation rate constants as functions of the translational-rotational temperature T and the vibrational temperature T_v. The rate constant depends more strongly on T when T_v is low, and it depends more strongly on T_v when T is low. Quasibound reactant states contribute significantly to the rate constants, as do exchange processes at higher temperatures. We discuss two sets of runs in detail: an equilibrium test set in which $T = T_v$ and a nonequilibrium test set in which $T_v < T$. In the equilibrium test set, high-v and moderately-low-j molecules contribute most significantly to the overall dissociation rate, and this state specificity becomes stronger as the temperature decreases. Dissociating trajectories tend to result in a major loss of vibrational energy and a minor loss of rotational energy. In the nonequilibrium test set, as T_v decreases while T is fixed, higher-j molecules contribute more significantly to the dissociation rate, dissociating trajectories tend to result in a greater rotational energy loss, and the dissociation probability's dependence on v weakens. In this way, as T_v decreases, rotational energy appears to compensate for the decline in average vibrational energy in promoting dissociation. In both the equilibrium and nonequilibrium test sets, in every case, the average total internal energy loss in the dissociating trajectories is between 10.2 and 11.0 eV, slightly larger than the equilibrium potential energy change of N_2 dissociation. © *2015 AIP Publishing LLC.* [http://dx.doi.org/10.1063/1.4927571]

I. INTRODUCTION

Hypersonic flows, in which gas speeds exceed about five times the speed of sound, are of great interest in the aerospace science community. Such flows must be understood, for example, for the engineering design of spacecraft for planetary entry, scramjet-powered aircraft, and ballistic missile systems. In hypersonic aerodynamics, high-temperature reactions between chemical species of the gas play an important role, especially for the analysis of a shock layer, the region of fluid between a strong shock wave and a vehicle surface. In air, dissociation of species like diatomic nitrogen and oxygen is a particularly significant chemical process that must be considered for accurate aerodynamic simulations using computational fluid dynamics (CFD) and other tools.

The present study is concerned with dissociation of N_2, which is a key gas-phase chemical reaction in hypersonic flows in air. This work consists of three major phases. (1) An accurate potential energy surface (PES) is constructed using quantum mechanical electronic structure methods and surface fitting.[1] This PES describes chemical interactions between the species (N_2 and N) of interest. (2) The PES is used in molecular dynamics (MD) calculations to analyze individual chemical reactions at high temperatures and to calculate their rate constants. (3) The results generated by MD are implemented in macroscopic simulations using continuum or particle-based techniques. In this paper, we discuss research from phases (1) and (2) on the $N_2 + N_2 \longrightarrow N_2 + 2N$ and $N_2 + N_2 \longrightarrow 4N$ dissociation reactions. This work expands on earlier research we presented recently.[2]

Research on diatomic dissociation (and nitrogen dissociation specifically) has a long history. Many studies have viewed dissociation as a process of vibrational excitation to an unbound state. They used a simplified diatomic potential, such as a truncated harmonic oscillator or a Morse potential, to compute probabilities of transitions between vibrational

energy levels, which in turn could be used to determine reaction rate constants via a master equation, a local-equilibrium approximation, or further simplifications. Such studies became increasingly more sophisticated in the last several decades. In the simplest ladder-climbing framework,[3–5] it was assumed that vibrational excitation occurred only via single-quantum transitions and that dissociation occurred only from the highest vibrational energy level. Variations of this idea allowed for limited multi-quanta transitions, but only permitted dissociation from the highest few vibrational levels.[6,7] More advanced models discarded the second assumption of the ladder-climbing framework, i.e., they allowed for dissociation from any vibrational level, but still only permitted single-quantum transitions in the vibrational manifold.[3,8–11] In some of these works, it was assumed that dissociation was equally likely from any vibrational level.[8,9] Other researchers built into their models a preference for dissociation from high vibrational levels.[10,11] Indeed, several early works found evidence that dissociation caused significant depletion of the high vibrational levels (resulting in non-Boltzmann energy distributions), because molecules in such levels were favored to dissociate.[6,12,13] Finally, still more advanced models, such as the Morse potential model of Johnston and Birks with all transitions allowed,[3] the forced harmonic oscillator (FHO) framework of Adamovich *et al.*,[14–17] and the information-theoretic approach of Gonzales and Varghese,[18–20] permitted both multi-quantum transitions and dissociation from any vibrational level. We could also include in this category the analytic model of Macheret and Rich,[21] which assumes classical, impulsive collisions between molecules and a "threshold function" for the minimum translational energy needed for a dissociative collision.

Many of the models we have referenced here did not account for the influence of rotational energy on the probability of dissociation. However, the possible dangers of that assumption have been analyzed,[22–24] and some of the investigators cited above did include rotational effects in their models.[7,16,17,21]

Advances in quantum chemistry and scientific computing in recent years have allowed for the construction of highly accurate PESs. These, in turn, have enabled the simulation of dissociative collisions using molecular dynamics,[23,24] without the many simplifying assumptions inherent in most of the models outlined above. For example, several researchers have used MD and a master equation to study H_2 dissociation (due to collisions with various partners such as Ar, He, and H); these studies consider both vibrational and rotational effects.[23–29] Recently, the success of such methods spawned a new family of MD-based nitrogen dissociation studies.[2,30–35] The present article will expand on that literature. We use the quasiclassical trajectory (QCT) method for running dynamics.[36,37] This method involves several steps. First, reactant molecules are prepared in classical analogs of quantized initial states. Then, reactants are collided by solving Hamilton's equations of motion for a classical trajectory, governed by interatomic forces computed as the negative gradients (with respect to atomic coordinates) of the PES. Finally, after the collision is complete, product molecules are identified and analyzed. This process is repeated many times, with initial conditions sampled from appropriate probability distributions. Then, ensemble-averaged quantities like reaction rate constants are calculated. The method is called "quasiclassical" because the trajectory motion is computed classically, while the initial conditions are determined based on quantized rovibrational states.

A notable feature of many hypersonic flows is the presence of thermal nonequilibrium, i.e., regions of the flow in which the translational kinetic energy mode of the gas is not equilibrated with the rotational and/or vibrational internal energy modes.[38] Accurately accounting for thermal nonequilibrium has been a persistent challenge for computational hypersonic aerodynamics for decades. State-specific approaches, in which all rovibrational states of all species are treated distinctly, are not tractable for macroscopic aerodynamic simulations. Consequently, aerospace scientists have resorted to approximate models that attempt to characterize a fluid volume in which energy is preferentially stored in one or more of the energy modes. One strategy is to define three temperatures, which are allowed to all be different: a *translational temperature* T, a *rotational temperature* T_r, and a *vibrational temperature* T_v.[33,34] Formally, such a framework implies that each chemical species inside a fluid element is characterized by a Maxwell-Boltzmann distribution of relative translational kinetic energies at T, an approximately Boltzmann distribution of rotational internal energies at T_r, and an approximately Boltzmann distribution of vibrational internal energies at T_v. However, in order to be more broadly applicable, such models typically employ a generalized definition for effective temperature as a function of energy averages.[33,34] This allows T, T_r, and T_v to be defined even for non-Boltzmann energy distributions, which is useful (even though it cannot be justified by statistical-mechanical arguments).

In a nonequilibrium gas, it is often assumed that the translational and rotational energy modes equilibrate rapidly, while the vibrational energy mode equilibrates more slowly through a process of *vibrational relaxation*.[38,39] For example, if we define the mean free time as the average time between collisions, typical textbook assumptions are that translation equilibrates in 1–3 mean free times, rotation equilibrates in 2–10 mean free times, and vibration equilibrates in 10^3–10^6 mean free times.[40,41] Consequently, a widely used additional assumption of multi-temperature models (made either explicitly or implicitly) is that $T = T_r$, while T_v may be different, thus reducing the three-temperature model to a two-temperature one.[9,10,42–49] We will use the two-temperature model in the present study. However, we note that there is a growing literature challenging the accuracy of assuming effectively instantaneous equilibration between translation and rotation; such investigations consider *rotational relaxation* times to be significant.[33,34,50,51]

We stress the approximate nature of all these approaches. Rotational and vibrational internal energies are not separable according to either classical or quantum mechanics. Indeed, let ε_{int} be the total internal energy of a diatomic molecule with vibrational quantum number v and rotational quantum number j. Let ε_{vib} be the molecule's vibrational energy, and let ε_{rot} be its rotational energy, each defined according to some reasonable (but ultimately arbitrary) way to separate the kinds of motion. For any reasonable scheme, we should have

that ε_{int} is the sum of ε_{vib} and ε_{rot}, but all three quantities will depend on both v and j. That is, it is not possible to simultaneously define ε_{vib} as a function of v alone and ε_{rot} as a function of j alone. Thus, strictly speaking, the notion of distinct rotational and vibrational temperatures is ambiguous. Furthermore, even if one accepted the approximation that vibrational and rotational energies were separable, a two- or three-temperature model can only fully characterize a gas with Boltzmann distributions of the translational, rotational, and vibrational manifolds. In general, non-Boltzmann distributions may be only poorly parameterized by temperatures.[52,53] Despite these shortcomings, the two- and three-temperature models have been widely used in the engineering design of successful hypersonic vehicles.

Consequently, in the QCT study described here, we designed a two-temperature model to investigate how the dissociation process varies with the energy distributions in a gas in thermal equilibrium and nonequilibrium. Our goal here is to obtain benchmark nitrogen dissociation rate constants for a representative set of precisely defined thermal environments. Such analyses shed light on how nitrogen dissociation proceeds under realistic hypersonic flow conditions, and the numerical results for rate constants can be used in the next generation of macroscopic models for high-temperature aerodynamics.

The remainder of this paper is divided into sections. In Sec. II, we present the new potential energy surface for the N_4 system, which forms a crucial foundation for the MD simulations. In Sec. III, we review the methodology of QCT, including an exposition of the two-temperature model we designed. In Sec. IV, we note several features of the codes we used to run the trajectories and of the simulations we executed. We discuss results from both thermal equilibrium and nonequilibrium simulations in Sec. V, where we compare our results with past theoretical, experimental, and computational work, and where we make some comments on possible future work. Finally, in Sec. VI, we summarize conclusions.

II. IMPROVED POTENTIAL ENERGY SURFACE

In previous work,[1] we presented a potential energy function for the ground-state N_4 system based on least-squares fits to the many-body component of the electronic energies. The fits are based on permutationally invariant polynomials[54,55] in bond order variables, where the bond order variables are given by exponentials,

$$X_i = \exp\left[-(r_i - r_e)/a\right], \tag{1}$$

where r_i is an internuclear distance, r_e is the equilibrium bond length of N_2, and a is a nonlinear parameter of the fit. The nonlinear parameter and coefficients of the polynomials (which are linear fitting parameters) were fit to 16 435 energies calculated by the complete active space second-order perturbation theory (CASPT2) quantum mechanical electronic structure method,[56,57] with the maug-cc-pVTZ[58] basis set. Of these points, 9350 correspond to planar geometries and 7085 correspond to nonplanar geometries.

In the present work, we make two improvements on the previous fit. We noticed that the fit to nonplanar geometries could be improved significantly by adding more nonplanar points to the data set, and so the first improvement is that we added 99 new energies corresponding to nonplanar geometries. These new data are given in the supplementary material.[59]

The second improvement is a change of functional form. Further study of the method with bond order variables showed that the method using Eq. (1) can be improved. One reason for this is that different values of a are optimal for fitting different regions of the global surface. The potential in the strong interaction regions can be described best with a value of a close to 1.0 Å, as used in our original fit. But the near-asymptotic regions are better described by a value of a near 0.4 Å, which is close to the Morse curve[60] value. Using 1.0 Å there causes incorrect long-range behavior, which could cause errors in treating near-threshold or low-temperature processes, as was pointed out recently.[61] A way to circumvent this difficulty is to replace X_i by a mixed exponential-Gaussian (MEG) variable, defined in Eq. (2) below,

$$Y_i = \exp\left[-(r_i - r_e)/a - (r_i - r_e)^2/b\right]. \tag{2}$$

Here, a and b are nonlinear parameters that provide the necessary flexibility.

Figure 1 shows that for large distances, the MEG function lies close to an X_i curve that has a small a value, while for short internuclear distances, this new function approaches an X_i curve that has a large a value. Although the function turns down below 0.5 Å, this behavior does not affect the quality of our PES, since the energy of the surface is extremely high when any distance is this small.

Table I compares the errors of the original[1] and new fits; for the new fits, the a and b parameters were manually optimized to 1.0 Å and 1.5 Å^2, respectively. We see that the new fit has smaller errors in each energy range, and it has smaller errors for both planar and nonplanar geometries. An even more important result is that it eliminates the spurious long-range behavior. The latter is illustrated in Figure 2, which shows a comparison of our old exponential and new MEG fits against the electronic structure data for a sample

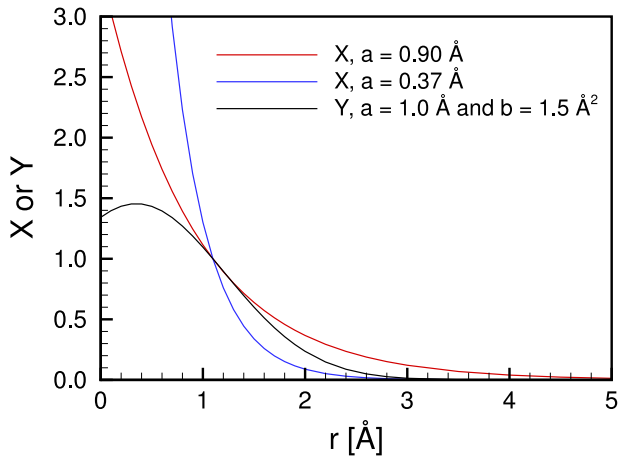

FIG. 1. One-dimensional comparison of exponential (X) and MEG (Y) variables along the r bond length. Note that $r_e = 1.098$ Å.

TABLE I. Comparison of the mean unsigned error (MUE) and root-mean-square error (RMSE) of the fitted potential energy surfaces with respect to CASPT2/maug-cc-pVTZ results for different data subsets. Energies are in kcal/mol.

		Exponentials		MEGs	
	Number of points	MUE	RMSE	MUE	RMSE
Subsets sorted by energy range					
$E < 100$	693	1.2	1.7	0.8	1.3
$100 \le E < 228$	1 974	2.4	4.1	2.1	3.8
$228 \le E < 456$	11 907	3.2	5.8	2.5	4.9
$456 \le E < 1000$	1 627	11.0	14.7	9.0	12.2
$E > 1000$	333	21.8	31.0	15.1	23.8
Subsets sorted by geometry					
Planar	9 350	4.6	9.0	3.7	7.3
Nonplanar	7 184	3.6	7.1	2.8	5.8
All data	16 534	4.2	8.2	3.3	6.7

long-range region. The high quality of the PES fit, as quantified by the low error values in Table I, is an important aspect of the current work. Indeed, in other QCT studies that included fitting of an analytic N_4 PES to electronic structure data, minimal[32] or no[35] quantitative statistics on fitting errors were reported.

The improved PES used for the present study is freely available online.[62] More details about the surface's structural features can be found in previous work.[1] We mention a few highlights here. First, the N_4 surface was designed with the N_3 surface as a subset; thus, the surface can be used to study both $N_2 + N_2$ and $N_2 + N$ interactions. Electronic energies from CASPT2 were calculated at geometries featuring the N_3 molecule and the tetrahedral form of N_4, which have also been studied by other researchers.[63–68] Some visualizations of relevant portions of the PES are depicted in Figure 3, corresponding to so-called H-shape and T-shape N_4 geometries.[1] Apparent are the repulsive walls of the potential and the flat regions corresponding to large intermolecular separation distances and to varying vibrational energy levels of the diatoms. Later in the paper, we will examine PES structure in the context of energy transfer mechanisms and trajectory pathways.

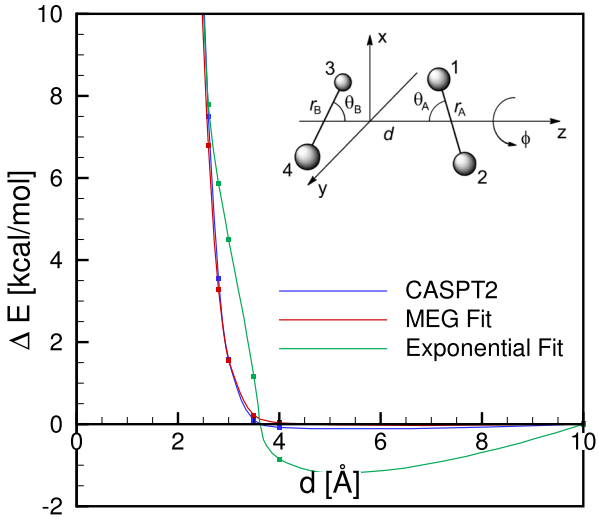

FIG. 2. Comparison of exponential and MEG fits against the CASPT2 data for the long-range region with tetrahedral geometry ($\theta_A = \theta_B = \phi = 90°$). Both N_2 molecules are at $r = 1.1$ Å $\approx r_e$.

III. QUASICLASSICAL TRAJECTORY METHODOLOGY IN A MULTI-TEMPERATURE FRAMEWORK

As we noted in Sec. I, the QCT method consists of several steps: preparation of reactants in classical analogs of quantized initial states, computation of the motion of a classical trajectory, and analysis of final states. We are studying the two related nitrogen dissociation reactions,

$$N_2(v_1, j_1) + N_2(v_2, j_2) \longrightarrow N_2(v', j') + 2N \tag{3}$$

and

$$N_2(v_1, j_1) + N_2(v_2, j_2) \longrightarrow 4N, \tag{4}$$

where v and j are vibrational and rotational quantum numbers, respectively. We do not consider electronically excited species. In this section, we discuss the QCT approach in detail, focusing on several features specific to our investigation of reactions (3) and (4).

A. Relative velocities and the reaction rate constant

The primary quantity of interest in this investigation is the *ensemble-averaged reaction rate constant* k, which we define in this investigation by

$$-\frac{d[N_2]}{dt} = \frac{1}{2}\frac{d[N]}{dt} = k_1[N_2]^2 + 2k_2[N_2]^2 \equiv k[N_2]^2, \tag{5}$$

where k_1 is the rate constant for the single-dissociation reaction (3), and k_2 is the rate constant for the double-dissociation reaction (4), each defined in the usual way.[69] Then, $k = k_1 + 2k_2$. In this formalism, k is an effective rate constant that describes the total rate of removal of N_2 and half the rate of production of N due to dissociation via $N_2 + N_2$ collisions. Such rates are useful because they can be used directly to calculate species concentrations in macroscopic simulations of high-temperature gases. Furthermore, by combining the effects of reactions (3) and (4) per Eq. (5), we can obtain a

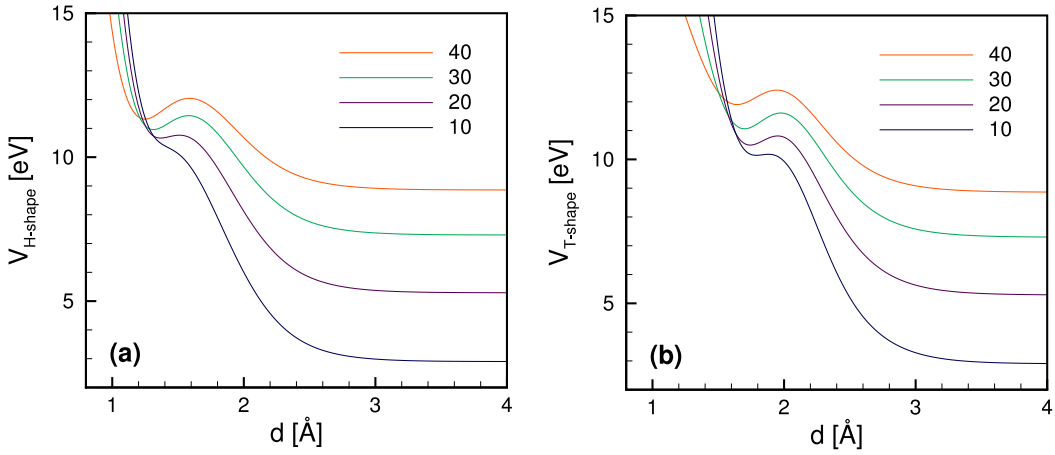

FIG. 3. Selected cuts through the N_4 PES. Shown are the potential energies for various geometries representative of two colliding N_2 molecules. We use the conventions in Fig. 2 to describe the geometries. For all cases, $r_B = 1.1$ Å $\approx r_e$, $\phi = 0°$, and $\theta_A = 90°$. For the "H-shape" geometry in (a), $\theta_B = 90°$. For the "T-shape" geometry in (b), $\theta_B = 0°$. The bond distance r_A is set to the separation distance for the outer turning point corresponding to the rotational quantum number $j = 0$ and the vibrational quantum number $v = 10$, 20, 30, or 40, as denoted in the legend. (These quantities are discussed in detail in Sec. III B.) Finally, the center-of-mass separation distance d is varied smoothly from a small value to 4 Å.

more comprehensive picture of energy transfer via dissociative $N_2 + N_2$ collisions, as discussed later in this paper.

In the QCT framework, we simulate a large number of representative collisions between N_2 collisions in an ensemble—characterized by one or more temperatures—and we use the results to calculate k. The rate constant for specific v and j and for a thermal distribution of relative kinetic energies at translational temperature T is the thermal average of the product of the relative speed v_r between the colliding N_2 molecules and the reaction cross section σ (which itself is a function of v_r, v, and j),[37,70]

$$k(T) = \frac{\langle v_r \sigma(v_r, v, j) \rangle_T}{2}. \tag{6}$$

The angular brackets $\langle \cdot \rangle_T$ in Eq. (6) indicate a thermal average over the distribution of relative velocities v_r at the temperature T.

The 1/2 factor in this expression is needed to properly treat "double-counting," which is unique to bimolecular reactions in which the two reactants are identical. The concept of double-counting is discussed at length in Ref. 38. Vincenti and Kruger illustrate the difficulty by noting that a collision between two identical species A and A terminates two free paths of A molecules; this is in contrast to a collision between two different species A and B, which terminates the free path of only one A molecule. To account for this difference, the authors introduce a "symmetry factor" χ, equal to 1 for distinct reactants and 2 for identical reactants.

For a three-temperature ensemble, with temperatures T, T_r, and T_v for translation, rotation, and vibration, respectively, the cross section must be averaged over the internal-temperature distributions characterized by T_r and T_v. We indicate such an average by an overbar. Then, Eq. (6) becomes

$$k(T, T_r, T_v) = \frac{\langle v_r \bar{\sigma}(v_r) \rangle_T}{2}. \tag{7}$$

Since we use a two-temperature model in which $T = T_r$, we will simply denote this quantity by $k(T, T_v)$. Further details of the ensemble average over T_r and T_v are presented below. For the thermal average over relative velocities, standard procedures yield the following:[37,69,70]

$$k(T, T_v) = \frac{1}{2} \pi b_{max}^2 \left(\frac{8 k_B T}{\pi \mu} \right)^{1/2} \int_0^\infty \int_0^{b_{max}} \bar{\bar{\mathscr{P}}}(E_r, b) \times \left(\frac{2b}{b_{max}^2} \right) \Lambda_r \exp(-\Lambda_r) \, db \, d\Lambda_r. \tag{8}$$

Here, μ is the reduced mass for the collision partners, k_B is the Boltzmann constant, E_r is the relative translational energy, $\Lambda \equiv E_r / k_B T$, b is the impact parameter, and b_{max} is the value of b beyond which there is a negligible probability of dissociation. Finally, $\bar{\bar{\mathscr{P}}}(E_r, b)$ is the probability of dissociation averaged over the vibrational and rotational quantum numbers and also over all other parameters (apart from E_r and b) that are needed to specify trajectory initial conditions. These parameters, such as the initial orientation of the collision partners, will be discussed in Sec. III D. A derivation of Eq. (8) is provided in the supplementary material.[59]

Eq. (8) forms the basis of our QCT analysis of reactions (3) and (4). The double integral in this equation is the overall *ensemble-averaged probability of reaction*, which we denote by $\langle \mathscr{P} \rangle_T$; it is the average of $\bar{\bar{\mathscr{P}}}(E_r, b)$ over the distributions of the relative translational energy and the impact parameter. (Note that we have dropped the double overbar from the expression $\langle \mathscr{P} \rangle_T$ to simplify the notation.) We seek to evaluate this quantity via Monte Carlo integration, by appropriate random sampling of the parameters E_r, b, and all other quantities necessary to characterize the initial state of a system of two colliding N_2 molecules.

B. Enumeration of quantized rovibrational states

To initialize a quasiclassical trajectory, we must assign vibrational and rotational quantum numbers, v and j, respectively, to each of the two reactant N_2 molecules. In this section, we describe an important prerequisite step: the enumeration of all possible rovibrational energy states of N_2. The procedure is well-known and is described in detail in Ref. 37. Here,

we will give a brief overview of the theory. We presented a similar overview as a part of an earlier project.[2] Also note that several other QCT studies of nitrogen dissociation have used a similar theoretical framework (with different potential energy surfaces).[30–35] In this discussion, ε_{int} denotes the total internal energy of a N_2 molecule.

In analyzing the quantized energy states of N_2, it is convenient to place the zero of energy at the minimum in the diatomic potential energy curve $V_D(r)$, where r is the internuclear distance. Then, the energy of a dissociated N_2 molecule is the dissociation energy D_e, which is 9.917 eV or 228.7 kcal/mol, for the fit to the CASPT2 calculations described in Sec. II. (The diatomic potential used in the fit has a functional form with nine parameters.[1]) We then define the effective potential energy for vibrational motion as a function of j as

$$V_{\text{D,eff}}(r,j) \equiv V_{\text{D}}(r) + \frac{j(j+1)\hbar^2}{2mr^2}, \tag{9}$$

where $\hbar$ is Planck's constant divided by 2π and m is the reduced mass for the diatom (not to be confused with μ, the reduced mass for the collision partners in a trajectory). Depending on the value of j, the $V_{\text{D,eff}}$ curve can have three possible shapes. For $j = 0$, it reduces to the potential V_{D}, which has a single minimum. For $0 < j \le j_{\max}$, it has a local minimum at small r (but larger than the equilibrium bond distance at $j = 0$), it has a local maximum at larger r, and it still approaches D_e as $r \to \infty$. The local maximum is due to the centrifugal barrier, caused by the second term in Eq. (9). In this case, let $\varepsilon_{\text{int,max}}(j)$ denote the energy at this local maximum. Finally, for the $j > j_{\max}$ case, $V_{\text{D,eff}}$ is purely repulsive, i.e., it has no local minimum (except at $r = \infty$).

With these definitions, we consider all of the quantum mechanical energy states of the diatom. In the $j = 0$ case, N_2 has bound states for $\varepsilon_{\text{int}} \lesssim D_e$. In the $0 < j \le j_{\max}$ case, N_2 has bound states for $\varepsilon_{\text{int}} \lesssim D_e$, it has quasibound states for $D_e \lesssim \varepsilon_{\text{int}} < \varepsilon_{\text{int,max}}(j)$, and it is unbound for higher ε_{int}. For the real N_2 molecule, the quasibound states have a finite lifetime because of tunneling through the centrifugal barrier; however, within the quasiclassical framework, they have an infinite lifetime and hence will be treated as bound. To make a list of all the bound and quasibound states, we should find, for each integer $j \le j_{\max}$, the eigenvalues ε_{int} of the vibrational Schrödinger equation,[71]

$$\left[-\frac{\hbar^2}{2m}\frac{d^2}{dr^2} + V_{\text{D,eff}}(r,j) - \varepsilon_{\text{int}}\right]\psi(r) = 0, \tag{10}$$

with homogeneous boundary conditions, where $\psi(r)$ is the wave function. We label the eigenvalues $\varepsilon_{\text{int}}(v,j)$, with $v = 0,1,2,\ldots,v_{\max}$ and $j = 0,1,2,\ldots,j_{\max}$. Note that $v_{\max}$ is a function of j. To approximate these eigenvalues, we can use the semiclassical Wentzel-Kramers-Brillouin (WKB)[37,71,72] approximation. Within this framework, we obtain the following:

$$v = -\frac{1}{2} + \frac{(2m)^{1/2}}{\pi\hbar}\int_{r-}^{r+}(\varepsilon_{\text{int}}(v,j) - V_{\text{D,eff}}(r,j))^{1/2}dr. \tag{11}$$

In Eq. (11), $r-$ and $r+$ are the internuclear distances at the inner and outer turning points on the effective potential energy curve that are associated with the (v,j) state.

This process ultimately yields a set of triples $(v,j,\varepsilon_{\text{int}})$, specifying all N internal energy states of the diatom. For convenience, we reference these states with a single index n, with $n = 1,2,3,\ldots,N$. In our implementation, we determined the local minimum and local maximum in an effective potential energy curve by using a two-part algorithm consisting of an initial bracketing step and a convergence step using inverse parabolic interpolation.[73,74] For finding inner and outer turning points, we used a simple bisection algorithm for finding roots.[73,74] For evaluating the integral in Eq. (11), we used a Gauss-Chebyshev quadrature method for numerical integration.[75]

For the diatomic potential used in the fit discussed in Sec. II, we found 9198 rovibrational states, with vibrational quantum numbers in the range 0–54 and rotational quantum numbers in the range 0–278. Of these, 7122 are truly bound states and 2076 are quasibound states that we treated as bound. As expected, the spacing between vibrational energy levels becomes smaller as v increases for fixed j, reflecting the anharmonicity of the potential energy curve. The spacing between rotational levels becomes larger as j increases for fixed v.

We note that in a recent investigation,[35] in which the same database of electronic structure data points used here was fitted to a different analytic form, different rovibrational states were predicted using the WKB method. Specifically, 9373 states were found in total, of which 6930 were bound and 2443 were quasibound, with v in the range 0–52 and j in the range 0–330. Since the underlying quantum chemistry data are identical, this difference is attributable to PES fitting quality, which is not sufficiently quantified in Ref. 35 to draw further conclusions.

C. The multi-temperature model

In Sec. III B, we described a procedure for enumerating all N rovibrational energy states of N_2, indexed by $n = 1,2,3,\ldots,N$. In this section, we discuss how we assign probabilities of occupation to those states, based on properties of the statistical ensemble under consideration and neglect of nuclear spin. Those probabilities are then used in the initialization of the quasiclassical trajectories.

First, consider a statistical ensemble characterized by a single rovibrational temperature T_{rv}. From statistical mechanics, the probability of selecting a diatom in internal state n is[76]

$$p(n) = p((v_n,j_n)) = \frac{(2j_n+1)\exp(-\varepsilon_{\text{int}}(v_n,j_n)/k_{\text{B}}T_{\text{rv}})}{Q_{\text{rovib}}(T_{\text{rv}})}. \tag{12}$$

Here, v_n and j_n are the quantum numbers corresponding to state n, and Q_{rovib} is the canonical rovibrational partition function, defined by[76]

$$Q_{\text{rovib}}(T_{\text{rv}}) = \sum_{n=1}^{N}(2j_n+1)\exp(-\varepsilon_{\text{int}}(v_n,j_n)/k_{\text{B}}T_{\text{rv}}). \tag{13}$$

The factor $(2j_n + 1)$ is the degeneracy of a state with rotational quantum number j_n. Note that with the analysis techniques described in Sec. III B, it is not necessary to use harmonic oscillator or rigid rotor analytic assumptions to evaluate $Q_{\text{rovib}}(T_{\text{rv}})$

in Eq. (12); since we have enumerated all allowable states, we can evaluate the partition function numerically.

As we explained in Sec. I, we are interested in modeling ensembles in which the distribution of internal energies cannot be modeled simply by one internal temperature. More specifically, we seek a model that can yield an approximately Boltzmann distribution of rotational energy levels at a rotational temperature T_r and an approximately Boltzmann distribution of vibrational energy levels at a (possibly different) vibrational temperature T_v. The non-separability of the rotational and vibrational energies precludes the construction of a model in which the rotational and vibrational energy distributions can be uniquely defined. However, we can design an approximate model as follows.

First, we must specify a rule for separating the internal energy of a diatom into two components: a vibrational energy ε_{vib} and a rotational energy ε_{rot}. A reasonable approach is to first define the vibrational energy of state (v, j) as the energy of the corresponding state with the given v and $j = 0$, i.e., at the ground rotational level. This is a common strategy, also used by Panesi *et al.*[33,34] Then, ε_{vib} is a function of v alone. We have the following definition:

$$\varepsilon_{vib}(v, j) \equiv \varepsilon_{int}(v, j = 0) = \varepsilon_{vib}(v), \tag{14}$$

where we measure ε_{int} from the minimum of the potential curve, not from the lowest-energy state, so that $\varepsilon_{vib}(0)$ is nonzero. (It is 0.147 eV.) Then, the rotational energy ε_{rot} is defined as the difference between the total internal energy and the vibrational energy. Thus, ε_{rot} is a function of both v and j. This is expressed below:

$$\varepsilon_{rot}(v, j) \equiv \varepsilon_{int}(v, j) - \varepsilon_{int}(v, j = 0). \tag{15}$$

We refer to the scheme defined by Eqs. (14) and (15) as the vibration-prioritized framework. We reiterate that other approaches are possible. For example, one could define the rotational energy first, as a function of j alone. Nevertheless, the vibration-prioritized framework is the most intuitive choice for approximately separating internal energies, because when v and j have low to moderate values, the spacing between vibrational energy levels is larger than the spacing between rotational energy levels. We use the definitions in Eqs. (14) and (15) for all work in this paper.

We computed the probability for state (v_n, j_n) as a product of two quantities: the probability of selecting the vibrational level v_n and the probability of selecting the state (v_n, j_n) conditional on having chosen the vibrational level v_n. The first of those probabilities is calculated based on the vibrational temperature T_v and the second based on the rotational temperature T_r. This scheme is expressed in Eq. (16) below:

$$\begin{aligned} p(n) = p((v_n, j_n)) &= \tfrac{1}{\eta}[\, p(v_n)]_{T_v}[\, p((v_n, j_n) \mid v_n)]_{T_r} \\ &= \frac{1}{\eta}\,[\, p(v_n)]_{T_v}\left[\frac{p((v_n, j_n))}{p(v_n)}\right]_{T_r}. \end{aligned} \tag{16}$$

If we now also define the canonical vibrational partition function (as we would if we had assumed that vibrational and rotational energies were separable),[38,76]

$$Q_{vib}(T_v) = \sum_{v=0}^{v_{max}} \exp(-\varepsilon_{vib}(v)/k_B T_v), \tag{17}$$

then we obtain the expanded form of Eq. (16) given below:

$$\begin{aligned} p(n) = p((v_n, j_n)) = \frac{1}{\eta}&\left(\frac{\exp(-\varepsilon_{vib}(v_n)/k_B T_v)}{Q_{vib}(T_v)}\right) \\ &\times\left(\frac{\left(\frac{(2j_n+1)\exp(-\varepsilon_{int}(v_n, j_n)/k_B T_r)}{Q_{rovib}(T_r)}\right)}{\left(\frac{\exp(-\varepsilon_{vib}(v_n)/k_B T_r)}{Q_{vib}(T_r)}\right)}\right). \end{aligned} \tag{18}$$

Note, crucially, that Eq. (18) reduces exactly to Eq. (12) when $T_r = T_v$. We emphasize that Eq. (12) is physical, but Eq. (18) is not. Rather, we have argued that Eq. (18) is a reasonable model for hypothetical ensembles that can be characterized by distinct rotational and vibrational temperatures. Notice that we have introduced a normalization constant η in Eqs. (16) and (18), which is necessary to ensure that the sum of all the probabilities is 1 when $T_r \neq T_v$. Obviously, $\eta = 1$ when $T_r = T_v$. Among all the cases, we considered in this project, η ranged from 0.95 to 1.10.

To illustrate the flexibility of the two-internal-temperature model, consider Figure 4. Here, we have prepared three statistical ensembles of N_2 molecules. In the first ensemble, T_r

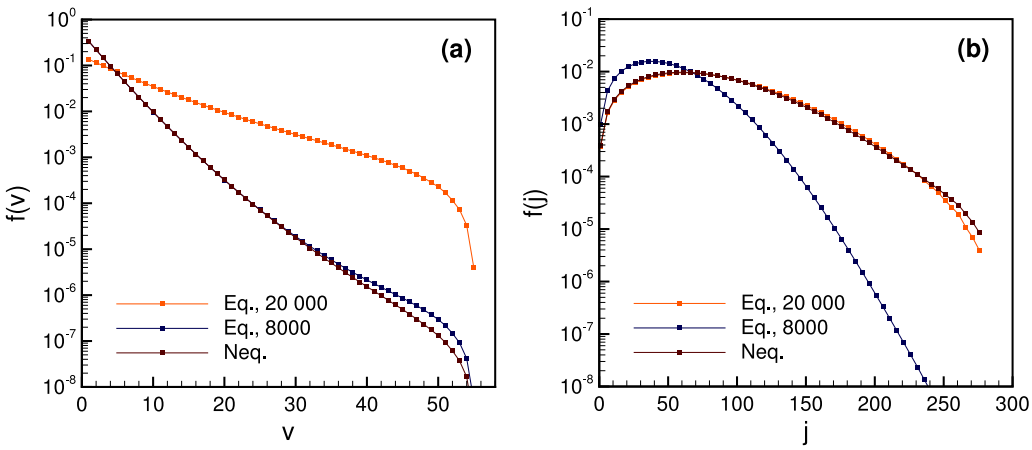

FIG. 4. Examples of probability density functions (PDFs) of the vibrational and rotational quantum numbers v and j, respectively, computed using the two-internal-temperature model of Eq. (18). (a) gives PDFs of v, and (b) gives PDFs of j. Three cases are shown in each plot: an equilibrium case in which $T_r = T_v = 20\,000$ K, an equilibrium case in which $T_r = T_v = 8000$ K, and a nonequilibrium case (Neq.) in which $T_r = 20\,000$ K and $T_v = 8000$ K.

$= T_v = 20\,000$ K. In the second, $T_r = T_v = 8000$ K. Finally, in the third, $T_r = 20\,000$ K and $T_v = 8000$ K. (Note that the translational temperature T is not relevant in this plot.) We give the probability density functions (PDFs) of v and j for each case. The first two ensembles represent cases of thermal equilibrium. As we discussed above, they are exactly described by Eq. (12) from statistical mechanics. The third ensemble represents a nonequilibrium case with $T_v < T_r$, a situation representative of vibrationally relaxing gases downstream of shock waves in hypersonic flows. Notice in Figure 4(a) that the PDF of v for the third ensemble is approximately equivalent to the corresponding PDF for the second ensemble; these two ensembles have the same vibrational temperature. Likewise, in Figure 4(b), the PDF of j for the third ensemble is approximately equivalent to the corresponding PDF for the first ensemble; these two ensembles have the same rotational temperature. This example supports the claim that Eq. (18) is effective at separating the distributions of rotational and vibrational energies in the way we desired. The model is not perfect; however, notice the slight divergence from the Boltzmann distributions in the third case at high v and j. As one might expect, we observed that this discrepancy generally becomes more significant as the difference between T_r and T_v increases in magnitude. The difference of 12 000 K in the nonequilibrium case shown here is relatively large among the cases we considered in this project.

D. Initial coordinates and velocities of reactants

In this section, we elaborate on how we initialize a quasiclassical trajectory, building on our discussion in Secs. III A–III C. The initial conditions are the Cartesian positions and velocities of the four N atoms in the system before the collision. We can specify these values using 18 (=6 × 4 − 6) parameters.

Two of these we have already discussed in Sec. III A. The relative translational kinetic energy E_r can be used to define a relative velocity between the centers of mass of the two reactants. Without loss of generality, we align the relative velocity vector with the z axis in our simulation reference frame. The impact parameter b is used to define an initial separation between the centers of mass of the reactants along the x axis, again without loss of generality. We set the separation along the y axis to be zero and along the z axis to be large enough so that the initial intermolecular forces between the reactants are negligible. Procedures for selecting E_r and b correctly are discussed in Ref. 37.

We next consider how to specify the orientation and initial velocities of the atoms of each N_2 molecule in their own center-of-mass reference frames. For each molecule, we first randomly select a quantized rovibrational state (v, j) per Eq. (18). We use the rotational quantum number j to set the magnitude of the classical internal angular momentum $\mathbf{J}$ of the diatom, based on the following semiclassical correspondence from quantum mechanics:[37,71]

$$\mathbf{J} \cdot \mathbf{J} = j(j+1)\hbar^2. \tag{19}$$

The vibrational quantum number v is used to set the initial separation distance between the two atoms. Following the suggestions in Ref. 37, we initialize the diatom at either its inner or outer turning point. Then, we determine a random phase angle ξ, with $0 \le \xi \le 2\pi$. This is used to determine a drift time for the molecule, i.e., an amount of time for the molecule to vibrate before the start of the trajectory, in order to reach a randomized point in its vibrational period. Next, we specify the orientation of the diatom's axis of symmetry using two randomly selected angles θ and ϕ. Finally, we use yet another randomly selected angle α to specify the initial orientation of the diatom's internal angular momentum vector, perpendicular to its central axis. These six parameters v, j, ξ, θ, ϕ, and α, all selected by Monte Carlo sampling, fully specify the initial conditions for the diatom in its center-of-mass frame. Further discussion of exactly how these six parameters can be converted into Cartesian positions and velocity components can be found in the references.[37,69,77]

E. Stratified sampling and uncertainty quantification

We turn in this section to the problem of evaluating an ensemble-averaged probability of dissociation $\langle \mathscr{P} \rangle_T$ from a large batch of quasiclassical trajectories. We need to evaluate the right-hand side of Eq. (8). This requires integrating over appropriate distributions for the relative translational kinetic energy E_r, the impact parameter b, the reactant internal rovibrational states, and all other parameters that we identified in Sec. III D. Fortunately, the rapid convergence of Monte Carlo methods makes tractable the numerical evaluation of the highly multidimensional integral in Eq. (8).

From Eq. (8), b must be sampled so that the probability of selecting an impact parameter in the interval (b, db) is $2\,b\,db/b_{max}^2$, for $0 \le b \le b_{max}$. We used stratified sampling[37] for this. For a given set of temperatures, we compute trajectories in batches. In each batch, we sample b from the interval $(0, b_{max})$ with a different value of b_{max}. For example, a typical run included six batches, with $b_{max} = 1, 2, \ldots, 6$ Å. The trajectories from all of the batches are then sorted into nonoverlapping intervals of b, which we call integration strata. Then, the evaluation of the integral in Eq. (8) is done in a piecewise fashion, with appropriate weighting for each stratum. In our research, we only partitioned the integral in Eq. (8) into strata based on the impact parameter. For all other integration parameters, we sampled without weights.

To quantify this procedure, we follow the exposition of Ref. 37. Suppose that we have calculated several batches of trajectories and have sorted the results into K integration strata indexed by $\kappa = 1, 2, \ldots, K$. Each stratum is defined by a minimum impact parameter value b_κ^- and a maximum value b_κ^+, and we assume that the strata are listed in increasing order so that $b_1^- = 0$ Å and $b_K^+ = b_{max}$. Then, each stratum is associated with a fraction $\mathscr{V}_\kappa$ of the total integration volume in b,

$$\mathscr{V}_\kappa = \frac{(b_\kappa^+)^2 - (b_\kappa^-)^2}{b_{max}^2}. \tag{20}$$

The sum of the $\mathscr{V}_\kappa$ is 1. We can interpret the $\mathscr{V}_\kappa$ values as weights on the contributions to $\langle \mathscr{P} \rangle_T$ from each of the strata. Let $\mathscr{N}_\kappa$ and $\mathscr{N}_{d,\kappa}$ denote the total number of trajectories and the number of dissociative trajectories in stratum κ. Then, assuming that we have used the correct probability distributions for all other

integration parameters, we have the following relation:[37]

$$\langle \mathscr{P} \rangle_T \cong \sum_{\kappa=1}^{K} \mathscr{V}_\kappa \frac{\mathscr{N}_{\mathrm{d},\kappa}}{\mathscr{N}_\kappa}. \tag{21}$$

By substituting this value for the integral in Eq. (8), we obtain the ensemble-averaged dissociation rate constant k.

Importantly, we also have the following formula for the one-standard-deviation statistical error on this Monte Carlo estimate for $\langle \mathscr{P} \rangle_T$:[37]

$$\Delta\langle \mathscr{P} \rangle_T \cong \left(\sum_{\kappa=1}^{K} \mathscr{V}_\kappa^2 \left(\frac{\mathscr{N}_{\mathrm{d},\kappa}(\mathscr{N}_\kappa - \mathscr{N}_{\mathrm{d},\kappa})}{\mathscr{N}_\kappa^3} \right) \right)^{1/2}. \tag{22}$$

We will use Eq. (22) to calculate statistical uncertainties throughout this paper. Note that this formula accounts only for statistical errors in the Monte Carlo integration; it does not include other sources of error, such as errors from fitting the PES to the CASPT2 data, from the lack of exact energy conservation in numerically integrated trajectories, and from the fundamental assumption of classical motion of the colliding atoms.

Finally, note that Eqs. (21) and (22) were derived specifically for the calculation of an ensemble-averaged probability of dissociation. However, the same formulas apply for determining the averaged probability of any event of interest that either does or does not occur in each trajectory; we simply replace $\mathscr{N}_{\mathrm{d},\kappa}$ with the number of trajectories $\mathscr{N}_{\mathrm{ev},\kappa}$ in which the event occurred. For example, we may be interested in trajectories that featured a single dissociative event and whose molecular product had an internal energy within a specified range. Thus, we will make extensive use of Eqs. (21) and (22) to investigate the dissociation process in detail.

IV. SIMULATIONS

Using the potential energy surface described in Sec. II and the methods described in Sec. III, we proceeded to compute quasiclassical trajectories to study reactions (3) and (4) under various conditions. We chose five temperatures: 8000, 10 000, 13 000, 20 000, and 30 000 K. We varied both the translational-rotational temperature T and the vibrational temperature T_v across the five values. In this process, we carried out a total of 25 runs, which are summarized in Table II. Notice that we generally ran more trajectories at lower temperatures, at which dissociation probabilities are lower and more trajectories are needed to obtain meaningful statistics. In total, over 2.4×10^9 trajectories were calculated.

TABLE II. Number N (in $\times 10^6$) of quasiclassical trajectories computed for each combination of the translational-rotational temperature T and vibrational temperature T_v. Temperatures are in K.

		T_v				
N		8000	10 000	13 000	20 000	30 000
	8 000	400	105	60	28	24
	10 000	320	96	70	28	24
T	13 000	240	96	56	24	16
	20 000	240	96	70	40	16
	30 000	180	96	70	24	16

TABLE III. Statistics on energy conservation in trajectories as a function of the Verlet integrator time step dt. Each row corresponds to a run of 8×10^6 trajectories with $T = T_\mathrm{v} = 30\,000$ K. For each case, we give the dissociation rate constant k and two statistics on the total energy deviation ΔE_tot from each trajectory: the maximum value and the average value (across all trajectories in the run). Time is in fs, k is in 10^{-11} cm^3 molecule^{-1} s^{-1}, and ΔE_tot values are in meV. See Sec. V for a description of the notation used to describe statistical uncertainty in k.

		Statistics on ΔE	
Δt	k	Maximum	Average
0.01	8.53(1)	0.587	0.0408
0.02	8.53(1)	1.68	0.163
0.05	8.50(1)	11.2	1.02
0.10	8.46(1)	49.6	4.07
0.20	8.41(1)	164.0	16.2
0.50	8.15(1)	1070.0	100.0
1.00	8.28(2)	6090.0	408.0

The trajectories themselves were computed with a Verlet integrator.[78] For the purposes of terminating a dissociating trajectory, a molecular bond is considered broken if it exceeds 10 Å. A non-dissociating trajectory is terminated if, after the collision, four out of the six internuclear distances in the system exceed 15 Å.

To determine an appropriate integration time step Δt for the runs, we first conducted several tests to understand how the time step affected energy conservation in a trajectory. Results from some of these studies are given in Table III. One needs a smaller time step when velocities are higher, so we conservatively chose $T = T_\mathrm{v} = 30\,000$ K for the test. For the tests summarized in Table III, we ran conservatively large batches of 8×10^6 trajectories each, varying Δt from 0.01 fs to 1 fs. For every trajectory, we calculated the magnitude of the energy deviation, defined as the difference between the largest and smallest total energy E_tot values calculated during the trajectory. E_tot is equal to

$$E_\mathrm{tot} = V(\mathbf{x}_1, \ldots, \mathbf{x}_4) + \sum_{i=1}^{4} \left(\frac{1}{2} m_i |\mathbf{v}_i|^2 \right), \tag{23}$$

where $\mathbf{x}_i$ and $\mathbf{v}_i$ denote the position and velocity vectors for atom i, V is the total potential energy in the system, and m_i is the mass of atom i. We then computed statistics on the set of values $\Delta E_\mathrm{tot} = E_\mathrm{tot,max} - E_\mathrm{tot,min}$ for each trajectory. As expected, both the maximum and average values of ΔE_tot increase as Δt increases. However, the change in the quantity of interest k is relatively small; the variation in k between the runs at low Δt is of the same order of magnitude as the one-standard-deviation statistical error. Considering that the choice of Δt has a major effect on the cost of the trajectory calculations, we decided to use $\Delta t = 0.05$ fs for all of our production runs. This provides a reasonable compromise between high accuracy and high efficiency.

A combined Fortran 90 and C code was written to perform the calculations. The code was parallelized with MPI. All large datasets were stored using the Hierarchical Data Format 5 (HDF5),[79] which improved computational efficiency and

streamlined the organization of our data. For random number generation, we used the multiplicative lagged Fibonacci generator of the Scalable Parallel Random Number Generators (SPRNG) library.[80] The simulations were run on supercomputing resources within the Candler group. Typical calculations used between 50 and 1000 cores.

V. RESULTS AND DISCUSSION

In this section, we analyze results from the 25 runs that we described in Sec. IV. Several conventions are used throughout this section. When reporting a one-standard-deviation statistical error for a quantity, we use parentheses to indicate the magnitude of the deviation in the last digit of the quantity. For example, the expression $1.23(4) \times 10^{-10}$ is equivalent to $1.23 \pm 0.04 \times 10^{-10}$. PDFs for a property of reactive trajectories are denoted by f. A vertical line | indicates a conditional probability, per standard conventions. For convenience, we use the abbreviation *dissoc* to mean any dissociation event, i.e., a trajectory that resulted in at least one dissociated nitrogen molecule. Finally, we reiterate that the reactant-ensemble translational and rotational temperatures, T and T_r, respectively, were equal for all simulations in this research; accordingly, we call T the translational-rotational temperature.

A. Dissociation rate constants

The ensemble-averaged dissociation rate constants k, computed from Eq. (8), are given in Table IV as a function of T and T_v. Recall that these rate constants, per Eq. (5), account for the destruction of molecular nitrogen from both single-dissociation and double-dissociation collisions between pairs of N_2 diatoms. The data are visualized in two different forms in Figure 5. We observe that k varies more rapidly with T when T_v is low. Consider, for example, that the rate constant increases much more rapidly with T when T_v is fixed at 8000 K than when T_v is fixed at 30 000 K. Likewise, k varies more rapidly with T_v when T is low. For example, observe that the rate constant increases much more rapidly with T_v when T is fixed at 8000 K than when T is fixed at 30 000 K.

In Figure 6, we compare data from Table IV with past research. Figure 6(a) compares our $T = T_v$ thermal equilibrium results with earlier studies. We include the experimental findings of Byron,[81] Appleton,[82] and Hanson and Baganoff[83] and the QCT-based results from Jaffe *et al.*[32] and Parsons *et al.*[35] Also included here are the most recent recommendations of Park,[43,44] which were based on compilations of earlier research. Our data agree most closely with the Park results at low temperatures, but diverge from his results at higher temperatures. To assist in comparing these various data, we provide a fit to our equilibrium rate constants in Eq. (24) below:

$$k_{eq}(T) = \left(\frac{4.50 \times 10^{-6}\ \text{cm}^3}{\text{molecule} \cdot \text{s} \cdot \text{K}^{-0.675}} \right) T^{-0.675} \times \exp\left(\frac{-1.17 \times 10^5\ \text{K}}{T} \right). \quad (24)$$

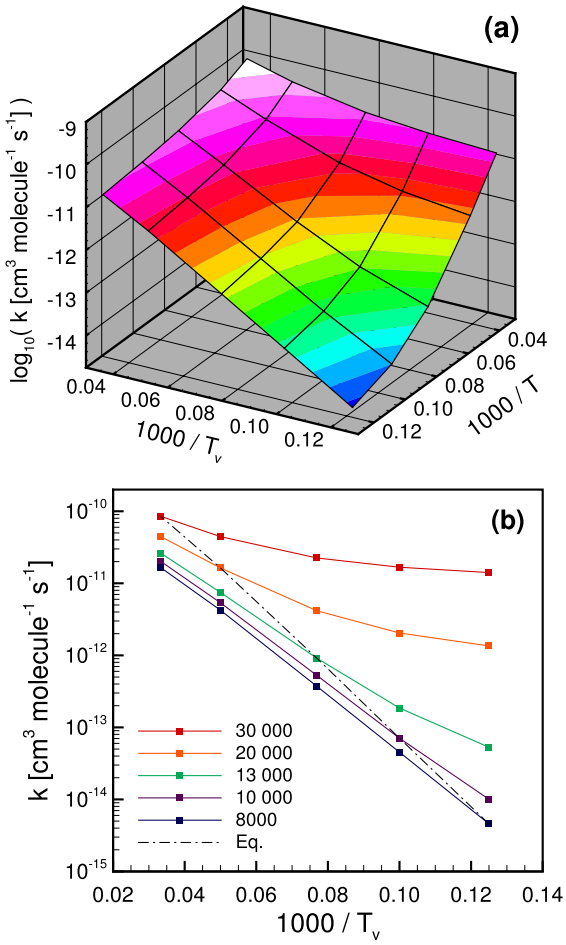

FIG. 5. Two depictions of dissociation rate constants k as a function of the translational-rotational temperature T and the vibrational temperature T_v. The data are from Table IV. In (b), variation in T_v corresponds to the horizontal axis, and the legend specifies lines of constant T. For clarity, an additional dashed-dotted black line is drawn through those equilibrium (Eq.) points at which $T = T_v$. For each data point in (b), the error bars, calculated using Eq. (22), are smaller than the symbol in size. Temperatures are in K.

TABLE IV. Dissociation rate constants k as a function of the translational-rotational temperature T and the vibrational temperature T_v. Temperatures are in K and k is in $\text{cm}^3\ \text{molecule}^{-1}\ \text{s}^{-1}$.

		T_v				
k		8000	10 000	13 000	20 000	30 000
	8 000	$4.6(1) \times 10^{-15}$	$4.53(7) \times 10^{-14}$	$3.72(3) \times 10^{-13}$	$4.23(1) \times 10^{-12}$	$1.650(3) \times 10^{-11}$
	10 000	$1.00(2) \times 10^{-14}$	$7.1(1) \times 10^{-14}$	$5.26(3) \times 10^{-13}$	$5.37(2) \times 10^{-12}$	$2.016(4) \times 10^{-11}$
T	13 000	$5.30(5) \times 10^{-14}$	$1.86(2) \times 10^{-13}$	$9.13(5) \times 10^{-13}$	$7.47(2) \times 10^{-12}$	$2.621(5) \times 10^{-11}$
	20 000	$1.352(2) \times 10^{-12}$	$2.043(5) \times 10^{-12}$	$4.160(9) \times 10^{-12}$	$1.633(3) \times 10^{-11}$	$4.457(7) \times 10^{-11}$
	30 000	$1.409(1) \times 10^{-11}$	$1.672(2) \times 10^{-11}$	$2.247(2) \times 10^{-11}$	$4.445(6) \times 10^{-11}$	$8.51(1) \times 10^{-11}$

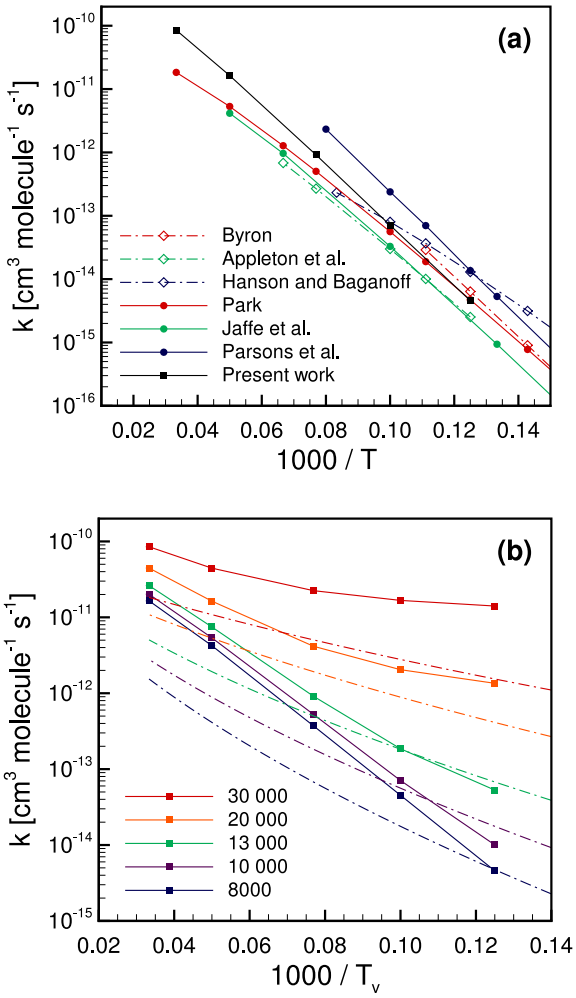

FIG. 6. Comparison of the dissociation rate constants k from Table IV with recent research. (a) Compares thermal equilibrium data with experimental data (shown in dashed-dotted lines) and computational or theoretical results (shown in solid lines). (b) Compares all data from Table IV (which is also presented in Figure 5(b)) with the Park two-temperature model. Our results are shown with symbols and solid lines, and the Park model results are shown in dashed-dotted lines. The value of T is indicated by color, as specified in the legend. Variation in T_v corresponds to the horizontal axis, while T is held fixed along each line. Temperatures are in K. See the text for corresponding references.

The parameters in this equation were determined via nonlinear least-squares fitting using MATLAB.[84]

In Figure 6(b), we repeat our depiction of the 25 rate constants shown in Figure 5(b), but now we also show rate constants computed along lines of constant T using the Park two-temperature model,[43,44] in which k is approximated as a function of the controlling temperature $T_a \equiv (TT_v)^{1/2}$. The Park model predicts values of k that are smaller than ours in almost all cases. The discrepancy is especially significant in those cases of large thermal nonequilibrium (when the magnitude of the difference between T and T_v is large). Agreement is best when both T and T_v are small.

B. Contributions to the rate constant from trajectory subsets

To understand the dissociation process in more detail, we report in this section on the percentage contributions to the dissociation rate constant k from various types of trajectories. We focus our attention on two sets of runs from the total 25. The first is an equilibrium test set, consisting of the five runs in which $T = T_v$, ranging from 8000 K to 30 000 K. The second is a nonequilibrium test set, consisting of the four runs in which T is fixed at 20 000 K and T_v varies from 8000 K to 20 000 K. The second set was chosen to shed light on ensembles representative of those in a vibrationally relaxing gas behind a shock, in which T_v is initially much less than T and equilibrates to T over time.

TABLE V. Percentage contributions k_κ/k to the dissociation rate constant, from trajectories with impact parameters b in different intervals. Data are from five equilibrium runs with $T = T_v$. Temperatures are in K, distances are in Å, and k_κ/k is given as a percentage.

		k_κ/k: $T = T_v =$				
b_{min}	b_{max}	8000	10 000	13 000	20 000	30 000
0	1	15.3	19.0	20.6	23.7	23.9
1	2	34.1	35.7	36.3	39.3	42.2
2	3	30.6	31.0	29.6	26.5	25.3
3	4	16.8	12.0	12.0	9.6	7.9
4	5	3.2	2.2	1.4	0.9	0.7
5	6	0.0	0.1	0.0	0.0	0.0

1. Dependence on impact parameter

We begin by examining the contributions to k from different integration strata in the impact parameter b, per our discussion of Eq. (21) in Sec. III E. Tables V and VI present the contributions from six different strata, each characterized by a b interval of width 1 Å. Figure 7 complements these tables. It gives the ratio of the probability of dissociation, conditional on the impact parameter, to the total probability of dissociation. This quantity $p(dissoc \mid b)/p(dissoc)$ can be interpreted as a scaled *opacity function*.[37,70] It satisfies the following relation, per arguments similar to those in the derivation of Eq. (8):[59]

$$\int_0^{b_{max}} \left(\frac{p(dissoc \mid b)}{p(dissoc)}\right)\left(\frac{2\,b}{b_{max}^2}\right) db = 1. \qquad (25)$$

It is important to remember that $p(dissoc \mid b)/p(dissoc)$ is not a probability density function itself, and its integral from 0 to b_{max} is not identically equal to unity; it should not be confused with the PDF $f(b \mid dissoc)$. Also note that the total probability

TABLE VI. Percentage contributions k_κ/k to the dissociation rate constant, from trajectories with impact parameters b in different intervals. The same conventions used in Table V are used here. Data are from four nonequilibrium runs with T fixed at 20 000 K and with T_v varied.

		k_κ/k: $T = 20\,000$, $T_v =$			
b_{min}	b_{max}	8000	10 000	13 000	20 000
0	1	44.3	39.9	32.9	23.7
1	2	36.6	37.7	38.7	39.3
2	3	15.8	17.7	21.3	26.5
3	4	3.2	4.4	6.5	9.6
4	5	0.1	0.3	0.6	0.9
5	6	0.0	0.0	0.0	0.0

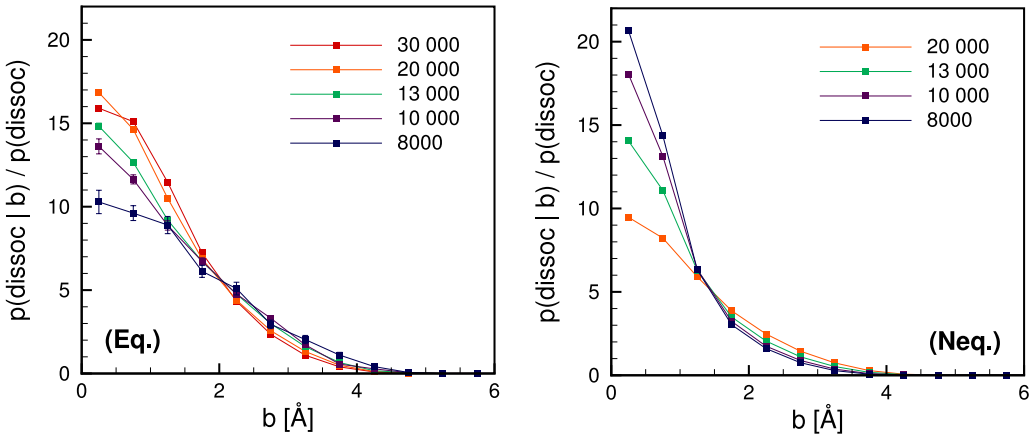

FIG. 7. Opacity functions scaled by the overall probability of dissociation. (Eq.) shows results from five equilibrium runs with $T = T_v$. The legend gives the equilibrium temperature. (Neq.) shows results from a set of four nonequilibrium runs with T fixed at 20 000 K and with T_v varied. The legend gives the value of T_v. The probability ratios in (Eq.) were computed based on trajectories with impact parameters in the range 0 Å $\le b \le$ 8 Å, while the probability ratios in (Neq.) were computed based on the range 0 Å $\le b \le$ 6 Å. See Tables V and VI for comparison. Temperatures are in K.

of dissociation $p(dissoc)$ varies by multiple orders of magnitude across the cases considered here.

First, consider Table V for the equilibrium test set. Notice that for each run in this set, the greatest contribution is from trajectories with impact parameters in the range [1, 2] Å. Furthermore, the normalized contribution from such trajectories becomes larger as the temperature increases. Additionally, the contribution from larger-impact-parameter trajectories, in which b is greater than 2 Å, becomes steadily smaller as the temperature increases. These trends are confirmed in the sharpening of the scaled opacity function plots for equilibrium conditions in Figure 7(Eq.) as the temperature increases. These observations are consistent with the well-known trend that the effective size of a molecule in a collision tends to decrease as the collision relative speed increases, because, intuitively, there is less time for the molecules to interact in glancing collisions. We do note that the probability ratio for collisions with b in the range [0.0, 0.5] Å is somewhat larger for the 20 000 K case than for the 30 000 K case. This suggests that at extremely high temperatures, there is less of a distinction between collisions below a certain small-impact-parameter threshold.

Now consider the nonequilibrium test set, corresponding to Figure 7(Neq.). Here, there is a clear sharpening of the scaled opacity function as the vibrational temperature is decreased and the translational-rotational temperature is held constant. This effect is also evident in Table VI, where we see that the normalized contribution to the rate constant from high-b trajectories decreases dramatically as T_v decreases. We can explain this phenomenon by noting that as the vibrational energy of a molecule decreases, the amount of energy that it must gain in a dissociative collision generally increases. Large energy transfers tend to result from small-b collisions, which are intuitively "harder." Consequently, it is reasonable to conclude that as T_v decreases while T is held constant, large-b collisions become less effective at inducing dissociation.

2. Dependence on event subtype

We have used the abbreviation *dissoc* to refer to a trajectory resulting in at least one dissociated N_2 molecule. It is instructive to look more carefully at exactly what outcomes are possible in a $N_2 + N_2$ collision and at how those different events contribute to the dissociation rate constant. To do so, first assume that we have indexed the four nitrogen atoms in the system from 1 to 4 such that the reactant diatoms are $N^{(1)}$–$N^{(2)}$ and $N^{(3)}$–$N^{(4)}$. Then, we identify five events of interest:

- *nonreactive* denotes a trajectory whose products have the same molecular bonds as the reactants. The products are the two diatoms $N^{(1)}$–$N^{(2)}$ + $N^{(3)}$–$N^{(4)}$.
- *simple-dissoc* denotes a trajectory whose products consist of two dissociated atoms and one diatom with the same molecular bond as one of the reactants. The products are either $N^{(1)}$–$N^{(2)}$ + $N^{(3)}$ + $N^{(4)}$ or $N^{(3)}$–$N^{(4)}$ + $N^{(1)}$ + $N^{(2)}$.
- *single-dissoc-swap* denotes a trajectory whose products consist of two dissociated atoms and one diatom that itself is composed of one atom from each of the two reactants. Two (out of four total) possibilities for the products are $N^{(1)}$–$N^{(3)}$ + $N^{(2)}$ + $N^{(4)}$ or $N^{(1)}$–$N^{(4)}$ + $N^{(2)}$ + $N^{(3)}$.
- *double-dissoc* denotes a trajectory in which the products consist of four dissociated atoms. There are no chemical bonds in the products.
- *metathesis* denotes a trajectory whose products consist of two diatoms, each of which contains one atom from each of the two reactants. There are no dissociated atoms. The products are either $N^{(1)}$–$N^{(3)}$ + $N^{(2)}$–$N^{(4)}$ or $N^{(1)}$–$N^{(4)}$ + $N^{(2)}$–$N^{(3)}$.

We will use these abbreviations throughout the remainder of this paper. Note that, in general, we expect the lowest-energy trajectories to be of the *nonreactive* type. Also, we expect *single-dissoc-swap*, *double-dissoc*, and *metathesis* trajectories to be typically of higher energy than *simple-dissoc* trajectories, because they require the breaking of both reactant molecular bonds rather than only one. Furthermore, when the frequency of *single-dissoc-swap*, *double-dissoc*, and *metathesis* events increases (relative to the frequency of *simple-dissoc* events), we expect an increase in the probability of $N_2 + N_2$ dissociation via *inelastic-partner collisions*, in which internal energy is

changed in both collision partners. Inelastic-partner collisions can be contrasted with *elastic-partner collisions*, in which dissociation of one particle occurs but the internal state of the other is unchanged. (For comparisons made in this paper, we will also use the term "elastic" loosely, to refer to internal state changes that are small but not exactly zero.)

To illustrate these concepts, Figure 8 gives visualizations of four representative trajectories, one for each of the event types except *nonreactive*. For each trajectory, the rovibrational states of the reactants were identical to those for the other three event types. Only the initial relative speed between the collision partners and their molecular and rotational orientations and vibrational phases were varied among the four plots of Figure 8. In all four cases, the vibration of the two reactants is apparent from the periodic structure in both the bond distances and the potential energy early in the trajectory. Figures 8(a) and 8(b) show a *simple-dissoc* and a *single-dissoc-swap* event, respectively. In both cases, there is one diatomic molecule in the products; this is evident from the smaller amplitude and approximately sinusoidal quality of the periodic potential energy change late in the trajectories. For the *double-dissoc* event depicted in Figure 8(c), the potential energy in the products becomes constant as the four atoms fly apart. For the *metathesis* event shown in Figure 8(d), large-amplitude periodic fluctuations in the potential energy resume late in the trajectory, after the two diatoms have formed again and begin to vibrate freely.

It is also instructive to compare the middle portion of the trajectories, when the actual collision occurs. For the case shown in Figure 8(a), diatom $N^{(3)}$–$N^{(4)}$ rebounds off its collision partner, with only small changes in its vibrational period, and r_{24} remains greater than about 2 Å throughout the trajectory. For the cases illustrated in Figures 8(b) and 8(d), we see the potential energy peak as both diatomic bonds break (at approximately the same time), then drop as the molecules move away from the steep repulsive wall at short interatomic distances. Also observe that the product diatom $N^{(2)}$–$N^{(4)}$ in 8(d) case has a much larger vibrational energy than either of the reactant molecules, indicative of the significant inelastic interaction that occurred in the collision. Finally, in the highest energy case shown in Figure 8(c), both reactant bonds break, again at approximately the same time, followed rapidly by a plateau in the potential energy at approximately twice the N_2 dissociation energy, which is 9.917 eV for the PES used here.

We turn next to a quantitative assessment of the contribution of each dissociation event subtype to the overall rate of destruction of N_2. For the purpose of counting events to

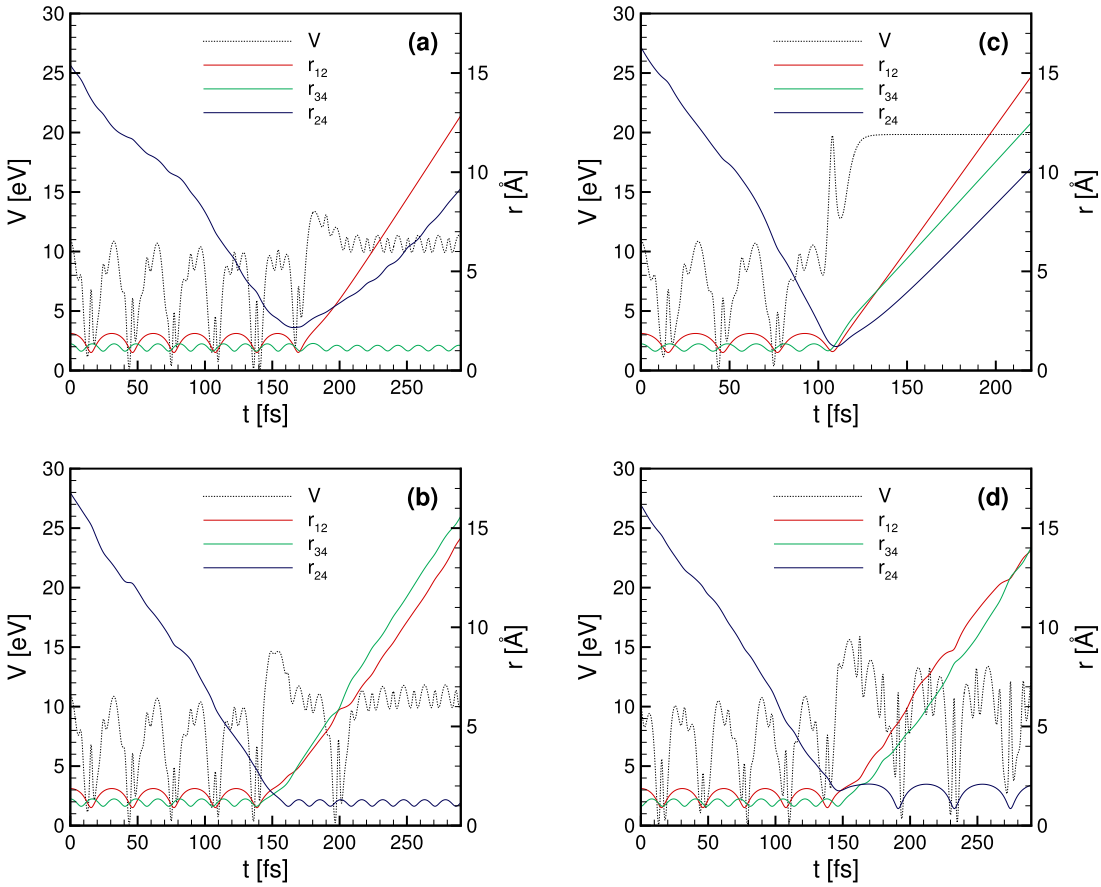

FIG. 8. Visualizations of four representative trajectories. Per the definitions in the text, each trajectory shown here is of a different type: (a) *simple-dissoc*, (b) *single-dissoc-swap*, (c) *double-dissoc*, and (d) *metathesis*. Dotted lines depict the total N_4 potential energy, and solid lines depict interatomic distances, where r_{ab} is the distance between atoms a and b, indexed from 1 to 4. The reactant diatoms are $N^{(1)}$–$N^{(2)}$ + $N^{(3)}$–$N^{(4)}$. Quantities are plotted versus elapsed time. For all four trajectories, $v_1 = 30$, $j_1 = 120$, $v_2 = 7$, and $j_2 = 78$. (Compare the mean v_1 and j_1 values for the $T = T_v = 20\,000$ K case reported in Table XI.) The collisions are head-on, i.e., $b = 0$ Å. The initial relative speed between the collision partners' centers of mass was 0.08 Å/fs for (a), 0.10 Å/fs for (b) and (d), and 0.15 Å/fs for (c). Random sampling was used for all other parameters.

TABLE VII. Percentage contributions k_{event}/k to the dissociation rate constant, from different types of dissociation events. The event types are defined in the text in Sec. V B 2. For comparison, a value of k_{event}/k is also provided for non-dissociative *metathesis* collisions. Data are from five equilibrium runs with $T = T_v$. Temperatures are in K and k_{event}/k is given as a percentage.

	k_{event}/k: $T = T_v =$				
Event	8000	10 000	13 000	20 000	30 000
simple-dissoc	99.1	97.0	92.5	80.5	69.2
single-dissoc-swap	0.9	3.0	7.5	18.9	28.2
double-dissoc	0.0	0.0	0.0	0.6	2.6
metathesis	1.1	2.3	3.3	5.5	6.5

calculate the overall dissociation rate constant k using Eqs. (8) and (21), we treat a single *double-dissoc* trajectory as if it was two *single-dissoc* trajectories. This is consistent with our discussion of the effective rate constant k in Eq. (5).

Table VII gives the contributions to k for the equilibrium test set from each of the three *dissoc* event subtypes: *simple-dissoc*, *single-dissoc-swap*, and *double-dissoc*. At low temperatures, almost all dissociation events are of the *simple-dissoc* subtype. As the temperature increases, the contribution from *single-dissoc-swap* events increases significantly. *double-dissoc* events are extremely rare in all cases, although they do play a slightly more significant role at higher temperatures. For the nonequilibrium test cases, Table VIII shows that the relative contribution from the three *dissoc* event subtypes remains approximately the same as T_v is increased with T held constant.

In Tables VII and VIII, we also give the effective rate constant for the (non-dissociative) *metathesis* event, as a percentage of k. In the equilibrium test set, this percentage is relatively small, but increases steadily with temperature. In the nonequilibrium test set, the relative rate constant for *metathesis* increases significantly as T_v is decreased while T is fixed. The increased frequency of *metathesis* events may indicate a greater role of inelastic-partner collisions (as defined above) in the dissociation process. We will return to this finding in Secs. V D–V E.

3. Dependence on type of reactant states

In Sec. III B, we described the difference between a truly bound and a quasibound state. Both types of states were considered in the reactant ensembles we used for our QCT calculations. Accordingly, each trajectory we ran can be classified into one of the three classes: (1) both reactant molecules were in bound states, a case that we denote by the name *bound-bound*, (2) one reactant was in a bound state and one was in a quasibound state (*bound-quasi*), or (3) both reactants were in quasibound states (*quasi-quasi*). We report in this section on the relative importance of each of these three classes of trajectories to the dissociation rate constant.

TABLE IX. Percentage contributions k_{state}/k to the dissociation rate constant from dissociating trajectories with different reactant initial states. The state classes are defined in the text in Sec. V B 3. The bottom row gives, for reference, the percentage $P(quasi)$ of quasibound molecules in the corresponding ensemble of reactants. Data are from five equilibrium runs with $T = T_v$. Temperatures are in K, and k_{state}/k and $P(quasi)$ are given as percentages.

	k_{state}/k: $T = T_v =$				
Reactant states	8000	10 000	13 000	20 000	30 000
bound-bound	36.4	39.4	39.9	41.7	39.8
bound-quasi	63.6	60.6	59.9	56.7	55.1
quasi-quasi	0.0	0.0	0.2	1.6	5.0
$P(quasi)$	0.001 56	0.0205	0.200	2.26	7.93

Table IX gives data for the equilibrium test set. Percentage contributions to the rate constant from the three different classes are given. Note the consistency in the relative contribution, across the temperature range, from the *bound-bound* class. The *bound-bound* trajectories account for ~40% of the rate constant, and trajectories featuring at least one quasibound reactant account for ~60% of the rate constant in all five runs. This trend is particularly interesting given that the population of (relatively high-energy) quasibound states in the reactant ensemble increases by multiple orders of magnitude from the cold to hot cases. For reference, we provide, in the last row of the table, the percentage $P(quasi)$ of quasibound states in the reactant ensemble. Evidently, quasibound molecules play a very significant role in the dissociation process. The same trend is maintained in the data from the nonequilibrium test set, which is reported in Table X. In all four runs, *bound-bound* trajectories account for ~40% of the rate constant and the other two classes of trajectories account for ~60%. We reiterate that the cases considered here are based on approximately Boltzmann distributions of initial translational, rotational, and vibrational energy states. In a real gas, depletion of

TABLE VIII. Percentage contributions k_{event}/k to the dissociation rate constant, from different types of dissociation events. The same conventions used in Table VII are used here. Data are from four nonequilibrium runs with T fixed at 20 000 K and with T_v varied.

	k_{event}/k: $T = 20\,000$, $T_v =$			
Event	8000	10 000	13 000	20 000
simple-dissoc	80.0	80.3	81.2	80.5
single-dissoc-swap	19.7	19.4	18.5	18.9
double-dissoc	0.2	0.3	0.3	0.6
metathesis	16.2	13.5	9.5	5.5

TABLE X. Percentage contributions k_{state}/k to the dissociation rate constant from dissociating trajectories with different reactant initial states. The same conventions used in Table IX are used here. Data are from four runs with T fixed at 20 000 K and with T_v varied.

	k_{state}/k: $T = 20\,000$, $T_v =$			
Reactant states	8000	10 000	13 000	20 000
bound-bound	39.2	39.1	39.7	41.7
bound-quasi	60.1	60.1	59.3	56.7
quasi-quasi	0.7	0.8	1.0	1.6
$P(quasi)$	0.682	0.817	1.12	2.26

high-energy-state populations may affect the relative contribution of quasibound molecules to the dissociation rate constant.

C. Initial states of the dissociating diatom in simple dissociation trajectories

In this section, we examine PDFs of the initial vibrational quantum number v_1, rotational quantum number j_1, and total internal energy $\varepsilon_{\text{int},1}$ of the reactant molecule $N_2^{(1)} = N^{(1)}$–$N^{(2)}$, in those *simple-dissoc* trajectories (as defined in Sec. V B 2) in which $N_2^{(1)}$ eventually dissociates. By restricting our attention to these types of dissociation events, we can gain information about which reactant molecules are favored to dissociate after colliding with another particle. However, it is important to remember that "non-swapping" dissociative trajectories make only a partial contribution to the rate constant at higher temperatures, as reported in Tables VII and VIII. For a "swapping" dissociative trajectory, it does not make sense to refer to the initial state of a molecule that eventually dissociates. Rather, both reactant molecules must be analyzed together. We will conduct such an analysis in Sec. V E.

Figure 9 depicts the PDFs of v_1, j_1, and $\varepsilon_{\text{int},1}$ for the equilibrium test set (denoted by Eq.) and for the nonequilibrium test set (denoted by Neq.). Consider the equilibrium

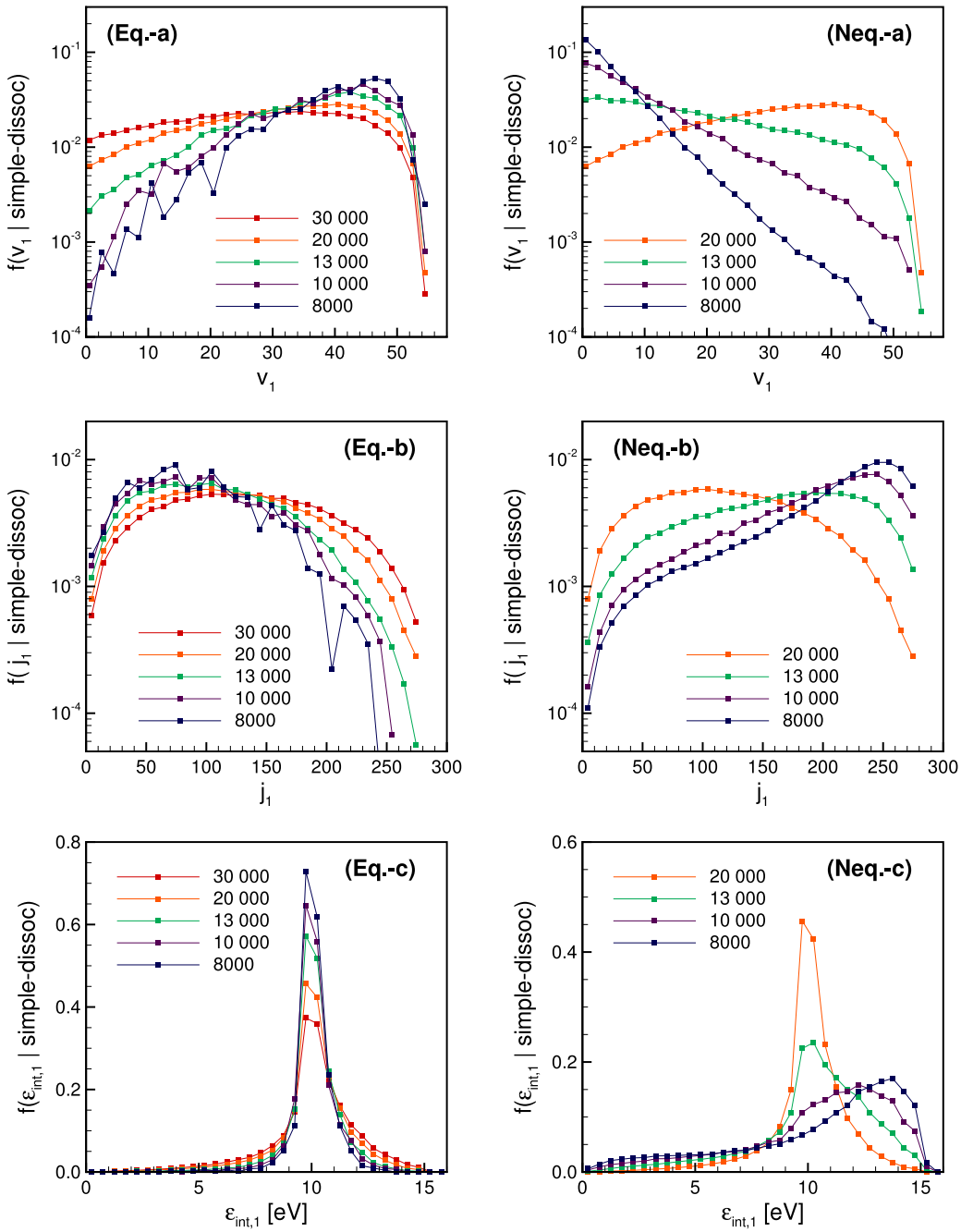

FIG. 9. PDFs of the initial vibrational quantum number v_1, rotational quantum number j_1, and total internal energy $\varepsilon_{\text{int},1}$ of the $N_2^{(1)}$ reactant molecule, for those *simple-dissoc* trajectories in which $N_2^{(1)}$ dissociates. (Eq.) denotes results from five equilibrium runs; the legend in these plots indicates the temperature $T = T_v$. (Neq.) denotes results from four nonequilibrium runs; the legend in these gives the vibrational temperature T_v while the translational temperature is held fixed at $T = 20\,000$. Note the difference in scales of the vertical axes of (Eq.-c) and (Neq.-c). Temperatures are in K.

TABLE XI. Statistics on properties of the first reactant molecule $N_2^{(1)}$, over all trajectories and over only *simple-dissoc* trajectories in which $N_2^{(1)}$ dissociates: v_1 and j_1 are the vibrational and rotational quantum numbers, respectively, and $\varepsilon_{\text{vib},1}$, $\varepsilon_{\text{rot},1}$, and $\varepsilon_{\text{int},1}$ are the vibrational, rotational, and total internal energies, respectively. Vibrational and rotational energies are defined by Eqs. (14) and (15). An overbar indicates an average over the entire ensemble of trajectories. Half-brackets $\lfloor \cdot \rfloor$ indicate an average over only those trajectories that result in a *simple-dissoc* event in which $N_2^{(1)}$ dissociates, i.e, $\lfloor x \rfloor$ means an average over the probability density function $f(x \mid \textit{simple-dissoc})$. Data are from five equilibrium runs with $T = T_v$. Temperatures are in K and energies are in eV. See Figure 9(Eq.) for comparison.

$T = T_v$	$\bar{v}_1$	$\bar{j}_1$	$\bar{\varepsilon}_{\text{vib},1}$	$\bar{\varepsilon}_{\text{rot},1}$	$\bar{\varepsilon}_{\text{int},1}$	$\lfloor v_1 \rfloor$	$\lfloor j_1 \rfloor$	$\lfloor \varepsilon_{\text{vib},1} \rfloor$	$\lfloor \varepsilon_{\text{rot},1} \rfloor$	$\lfloor \varepsilon_{\text{int},1} \rfloor$
30 000	10.2	95.7	2.77	2.46	5.23	26.7	132.0	6.26	3.78	10.0
20 000	7.01	78.4	2.00	1.76	3.76	30.1	120.0	6.91	3.11	10.0
13 000	4.03	61.4	1.25	1.15	2.40	34.3	107.0	7.69	2.36	10.1
10 000	2.83	53.0	0.929	0.877	1.81	36.7	98.1	8.10	1.96	10.1
8 000	2.09	46.9	0.725	0.700	1.43	38.8	91.6	8.43	1.62	10.1

results first. Several trends are evident: as the temperature decreases, the PDF of v_1 becomes more biased toward high vibrational quantum numbers and the PDF of j_1 becomes more biased toward moderately-low rotational quantum numbers. Likewise, we observe that at higher temperatures, the PDFs of both v_1 and j_1 are more uniform, with greater contributions from low-v and high-j molecules. These trends are maintained down to the coldest temperatures 10 000 K and 8000 K, although statistical data noise is more evident in those cases. The trends suggest that the relative contributions of high-v and moderately-low-j molecules to the overall dissociation rate become larger as the equilibrium temperature decreases. (Panesi *et al.* reach a similar conclusion in their recent QCT analysis of the $N_2 + N \longrightarrow 3N$ dissociation reaction.[33]) This finding is further substantiated by the data in Table XI: over the dissociating trajectories under consideration, the average value of v_1 decreases and the average value of j_1 increases with increasing equilibrium temperature. This trend in the average vibrational quantum number can be explained by the fact that if the relative translational energy in a collision is high, then less initial vibrational energy is typically needed to induce dissociation. Finally, note that the average value of v_1 over all molecules in the reactant ensemble increases with temperature, i.e., the trend in the average vibrational quantum number is reversed when the average is taken over only the dissociating trajectories instead of over the entire ensemble. These findings illustrate the shortcomings of simple ladder-climbing models and their variants, which assume that dissociation occurs only from the highest vibrational level[3–5] or the highest few vibrational levels.[6,7] Evidently, such assumptions become worse as the equilibrium temperature increases and dissociation from lower-v levels becomes more significant.

The observation that favoring of certain (v, j) states becomes stronger as the temperature decreases is also borne out in Figure 9(Eq.-c). Here, we see a clear pattern: if it eventually dissociates via a *simple-dissoc* event, then the molecule $N_2^{(1)}$ is very likely to have a total internal energy $\varepsilon_{\text{int},1}$ of ~10.0 eV. This favoring becomes significantly stronger as the temperature increases. (Again, note a similar trend in the results of Panesi *et al.* in their analysis of the $N_2 + N \longrightarrow 3N$ reaction.[33]) This behavior is also revealed in Table XI, where we see that the average of $\varepsilon_{\text{int},1}$ over the dissociating trajectories remains nearly constant at between 10.0 and 10.1 eV, even though the average over all molecules in the ensemble decreases with temperature. Note that this average is slightly more than the dissociation energy of N_2, which is 9.917 eV for the PES of Sec. II.

Next, we turn to results from the nonequilibrium test set, shown in Figure 9(Neq.) and in Table XII. A very different phenomenon is seen here, as the vibrational temperature drops from 20 000 K to 8000 K while the translational-rotational temperature is held fixed. As T_v decreases, we see that there is a greater contribution to the dissociation rate from low-v and high-j states. The average value of v_1 over the dissociating trajectories decreases, along with the average over all reactants in the ensemble. The average value of j_1 over the dissociating trajectories increases, while the average over all reactants stays approximately constant (since $T = T_r$ is being held constant). Both of these observations suggest that as T_v drops but T is held fixed, there is a greater probability that the dissociating trajectories will involve highly rotationally excited molecules. The role of vibrational energy lessens, in the sense that there is less of a bias for high-v states in the dissociative collisions. Indeed, notice that the PDFs in Figure 9(Neq.-a) become

TABLE XII. Statistics on initial properties of the first reactant molecule $N_2^{(1)}$ over all trajectories and over only *simple-dissoc* trajectories in which $N_2^{(1)}$ dissociates. The same conventions used in Table XI are used here. Data are from four runs with T fixed at 20 000 K, and with T_v varied. See Figure 9(Neq.) for comparison.

T_v	$\bar{v}_1$	$\bar{j}_1$	$\bar{\varepsilon}_{\text{vib},1}$	$\bar{\varepsilon}_{\text{rot},1}$	$\bar{\varepsilon}_{\text{int},1}$	$\lfloor v_1 \rfloor$	$\lfloor j_1 \rfloor$	$\lfloor \varepsilon_{\text{vib},1} \rfloor$	$\lfloor \varepsilon_{\text{rot},1} \rfloor$	$\lfloor \varepsilon_{\text{int},1} \rfloor$
20 000	7.01	78.4	2.00	1.76	3.76	30.1	120.0	6.91	3.11	10.0
13 000	4.01	77.6	1.25	1.79	3.04	19.0	160.0	4.69	5.53	10.2
10 000	2.82	77.2	0.929	1.79	2.73	10.7	187.0	2.88	7.52	10.4
8 000	2.09	76.9	0.726	1.79	2.53	5.87	202.0	1.73	8.78	10.5

qualitatively closer to a Boltzmann distribution as T_v drops, indicating a more uniform probability of dissociation from any v. This suggests that when $T_v \ll T$, the assumption of some early models that there is no preference for vibrational energy in dissociation[8,9] is roughly correct, if interpreted in the context of the two-temperature model. The sharpening of the PDFs in Figure 9(Neq.-b) with decreasing T_v also suggests the increasingly important role of rotational energy in determining trajectory outcomes when $T_v \ll T$. These observations are consistent with several earlier studies that argued that high-j states can play an important role in the dissociation process, particularly if there has been a depletion of vibrational energy from the ensemble.[13,21,23,24] For example, Macheret and Rich assert, using classical arguments, that (non-collinear) collisions between rotationally excited molecules should account for a larger fraction of all dissociation events in the $T_v \ll T$ case.[21] In such a situation, rotational energy compensates for the lack of vibrational energy in promoting dissociation.

The PDFs of total internal energy $\varepsilon_{\text{int},1}$ exhibit dramatic qualitative changes across the nonequilibrium runs. First, notice, from Table XII, that the average energy over the dissociating trajectories still remains very close to 10.0 eV, increasing only by a few percent as T_v decreases—a result remarkably consistent with the data in Table XI. However, the PDF of $\varepsilon_{\text{int},1}$ loses its sharp peak around 10.0 eV as T_v falls. There is a broadening out of the PDF and also a notable increase in the probability corresponding to very-high-energy (quasibound) molecules. From Figure 9(Neq.-b) and our discussion above, we expect those molecules to have a large rotational energy component.

D. Energy transfer to the dissociating diatom in simple dissociation trajectories

In Sec. V C, our focus was on the dissociating molecule in *simple-dissoc* trajectories. It is also instructive to analyze its collision partner, e.g., to study the molecule $N_2^{(2)} = N^{(3)}$–$N^{(4)}$ in simple dissociation trajectories in which $N_2^{(1)} = N^{(1)}$–$N^{(2)}$ dissociates. Such an analysis sheds light on the energy transfer mechanisms that cause dissociation. We will look in detail at two cases from the equilibrium test set and two cases from the nonequilibrium test set: a hot equilibrium case with $T = T_v = 20\,000$ K, a cold equilibrium case with $T = T_v = 10\,000$ K, a moderately nonequilibrium case with $T = 20\,000$ K and $T_v = 13\,000$, and a strongly nonequilibrium case with $T = 20\,000$ K and $T_v = 8000$ K.

First, consider Figure 10. PDFs are given of three different measures of energy transfer: the change in vibrational energy

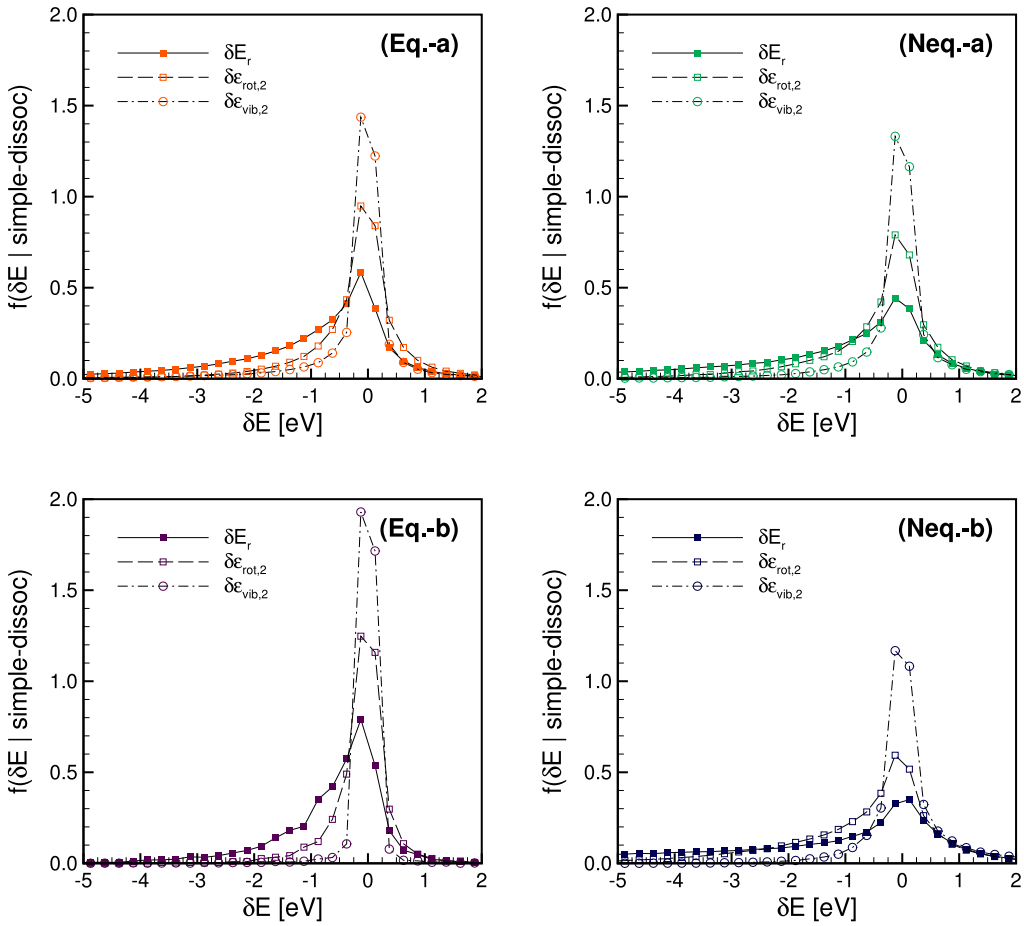

FIG. 10. PDFs of changes in vibrational and rotational internal energies of the undissociated diatom $N_2^{(2)}$, $\delta\varepsilon_{\text{vib},2}$, and $\delta\varepsilon_{\text{rot},2}$, respectively, and the change in relative translational energy δE_r between the two atom pairs' centers of mass, for those *simple-dissoc* trajectories in which $N_2^{(1)}$ dissociates. Four cases are represented: a hot equilibrium case in (Eq.-a), a cold equilibrium case in (Eq.-b), a moderately nonequilibrium case in (Neq.-a), and a strongly nonequilibrium case in (Neq.-b). Temperatures for these cases are given in Table XIII.

TABLE XIII. Statistics on energy transfer in *simple-dissoc* trajectories in which $N_2^{(1)}$ dissociates. Analyzed are the initial vibrational and rotational internal energies of the collision partner $N_2^{(2)}$, $\varepsilon_{\text{vib},2}$, and $\varepsilon_{\text{rot},2}$, respectively, and the initial relative translational energy E_r between the two atom pairs' centers of mass. Also considered are the changes in the corresponding quantities from the beginning to the end of the trajectory, denoted by $\delta\varepsilon_{\text{vib},2}$, $\delta\varepsilon_{\text{rot},2}$, and δE_r. Half-brackets $\lfloor\cdot\rfloor$ indicate an average over only those trajectories that result in a *simple-dissoc* event in which $N_2^{(1)}$ dissociates, i.e, $\lfloor x\rfloor$ means an average over the probability density function $f(x\,|\,\textit{simple-dissoc})$. Four cases were considered at the temperatures T and T_v specified. Temperatures are in K and energies are in eV. See Figure 10 for comparison, in which each subfigure corresponds to a row in the table as indicated.

Figures	T	T_v	$\lfloor\varepsilon_{\text{vib},2}\rfloor$	$\lfloor\varepsilon_{\text{rot},2}\rfloor$	$\lfloor E_\text{r}\rfloor$	$\lfloor\delta\varepsilon_{\text{vib},2}\rfloor$	$\lfloor\delta\varepsilon_{\text{rot},2}\rfloor$	$\lfloor\delta E_\text{r}\rfloor$
10(Eq.-a)	20 000	20 000	2.04	1.89	4.45	−0.217	−0.227	−1.17
10(Eq.-b)	10 000	10 000	0.949	0.985	2.34	−0.0491	−0.127	−0.656
10(Neq.-a)	20 000	13 000	1.33	2.11	5.23	−0.0603	−0.424	−1.62
10(Neq.-b)	20 000	8 000	0.773	2.40	6.39	0.174	−0.696	−2.28

of $N_2^{(2)}$, $\delta\varepsilon_{\text{vib},2}$, the corresponding change in rotational energy, $\delta\varepsilon_{\text{rot},2}$, and the change in relative translational energy, δE_r, between the $N^{(1)}$–$N^{(2)}$ and $N^{(3)}$–$N^{(4)}$ centers of mass. (Each of these changes is computed as the quantity in the products minus the quantity in the reactants. Also, note that δE_r is well-defined whether or not $N_2^{(1)}$ is dissociated.) We immediately notice that, in general, $\delta E_\text{r} < \delta\varepsilon_{\text{rot},2} < \delta\varepsilon_{\text{vib},2}$: notice the differences in the PDF maximums near $\delta E = 0$ and the differences in the probability densities at large-magnitude negative values. These observations are supported by numerical calculations of the PDF means, presented in Table XIII. Thus, the additional energy required for simple dissociation of $N_2^{(1)}$ appears to come primarily from translation, rather than from vibrational or rotational energy transfer from $N_2^{(2)}$ to $N_2^{(1)}$.

From Table XIII, both vibrational and rotational energy losses from $N_2^{(2)}$ increase in magnitude when the equilibrium temperature increases. As T_v decreases while T is held fixed, rotational energy loss increases significantly, but vibrational energy loss decreases. In fact, in the strongly nonequilibrium case, there is a tendency for $N_2^{(2)}$ to *gain* vibrational energy when $N_2^{(1)}$ dissociates, a behavior we would expect in nonreactive collisions as T_v equilibrates to T. The magnitude of rotational energy transfer in the strongly nonequilibrium case is over three times larger than in the hot equilibrium case. These trends in internal energy exchange should be noted alongside the discussion of *metathesis* events in Sec. V B 2. The trends support the claim that inelastic-partner collisions play an increasingly important role in dissociation as T_v decreases with T fixed, although translational energy transfer remains the dominant mechanism of dissociation.

We close this section with a reminder that, especially in the high-temperature cases, *simple-dissoc* trajectories only account for a fraction of the total number of dissociative trajectories. To analyze energy transfer due to all dissociation event subtypes, a more comprehensive approach is needed. This is the subject of Sec. V E.

E. Net changes in internal energies in dissociating trajectories

We will examine in this section how the internal energies in the four-nitrogen-atom system change from the reactants to the products in dissociating trajectories. More specifically, we will study the quantity,

$$\delta\varepsilon_\text{vib} = \varepsilon_\text{vib}^{(\text{products})} - \varepsilon_\text{vib}^{(\text{reactants})}, \tag{26}$$

where $\varepsilon_\text{vib}^{(\text{reactants})}$ is the sum of the vibrational internal energies of the two reactant molecules, and $\varepsilon_\text{vib}^{(\text{products})}$ is the vibrational internal energy in the products. For this definition, the vibrational energy of two dissociated atoms is zero; in the center-of-mass frame, all of the kinetic energy of the two separated atoms contribute to the system's relative translational kinetic energy. Thus, for a dissociating trajectory, $\varepsilon_\text{vib}^{(\text{products})}$ is either zero (for a *double-dissoc* event) or is the vibrational energy of the single N_2 product molecule (for a *simple-dissoc* or a *single-dissoc-swap* event). We define the quantities $\delta\varepsilon_\text{rot}$ and $\delta\varepsilon_\text{int}$ analogously to Eq. (26), for the rotational energy and the total internal energy, respectively.

The utility of Eq. (26) lies in its generality: this quantity can be defined for any $N_2 + N_2$ collision, regardless of the *dissoc* event subtype or even whether or not a reaction occurs. This is in contrast to the quantities $\delta\varepsilon_{\text{vib},2}$ and $\delta\varepsilon_{\text{rot},2}$, analyzed in Sec. V D. We thus hypothesize that by considering the quantity $\delta\varepsilon_\text{vib}$ and its analogues, we can study (with minimal restricting assumptions) how energy moves between different modes in the dissociating N_2 gas.

Figure 11(Eq.) and Table XIV show results from our investigation of internal energy changes in the equilibrium test set. We highlight several features. First, dissociating trajectories tend to result in a relatively large vibrational energy loss. A loss of about 10 eV is most likely. A loss of larger than 10 eV is extremely rare, but there is a non-negligible probability of smaller-magnitude losses. Second, these trajectories tend to result in a relatively small rotational energy loss. A loss of 0–1 eV is most likely, but there is a non-negligible probability of losses up to about 10 eV. Third, there is a very high probability that these trajectories result in a total internal energy loss of about 10 eV, just larger than the dissociation energy of one N_2 molecule. Furthermore, all three of these trends become sharper as the temperature decreases. Thus, the average (over dissociating trajectories) of $\delta\varepsilon_\text{vib}$ increases in magnitude and the average of $\delta\varepsilon_\text{rot}$ decreases in magnitude as the temperature decreases. The average of $\delta\varepsilon_\text{int}$ decreases slightly from −10.2 to −11.0 eV as the temperature increases from 8000 to 30 000 K.

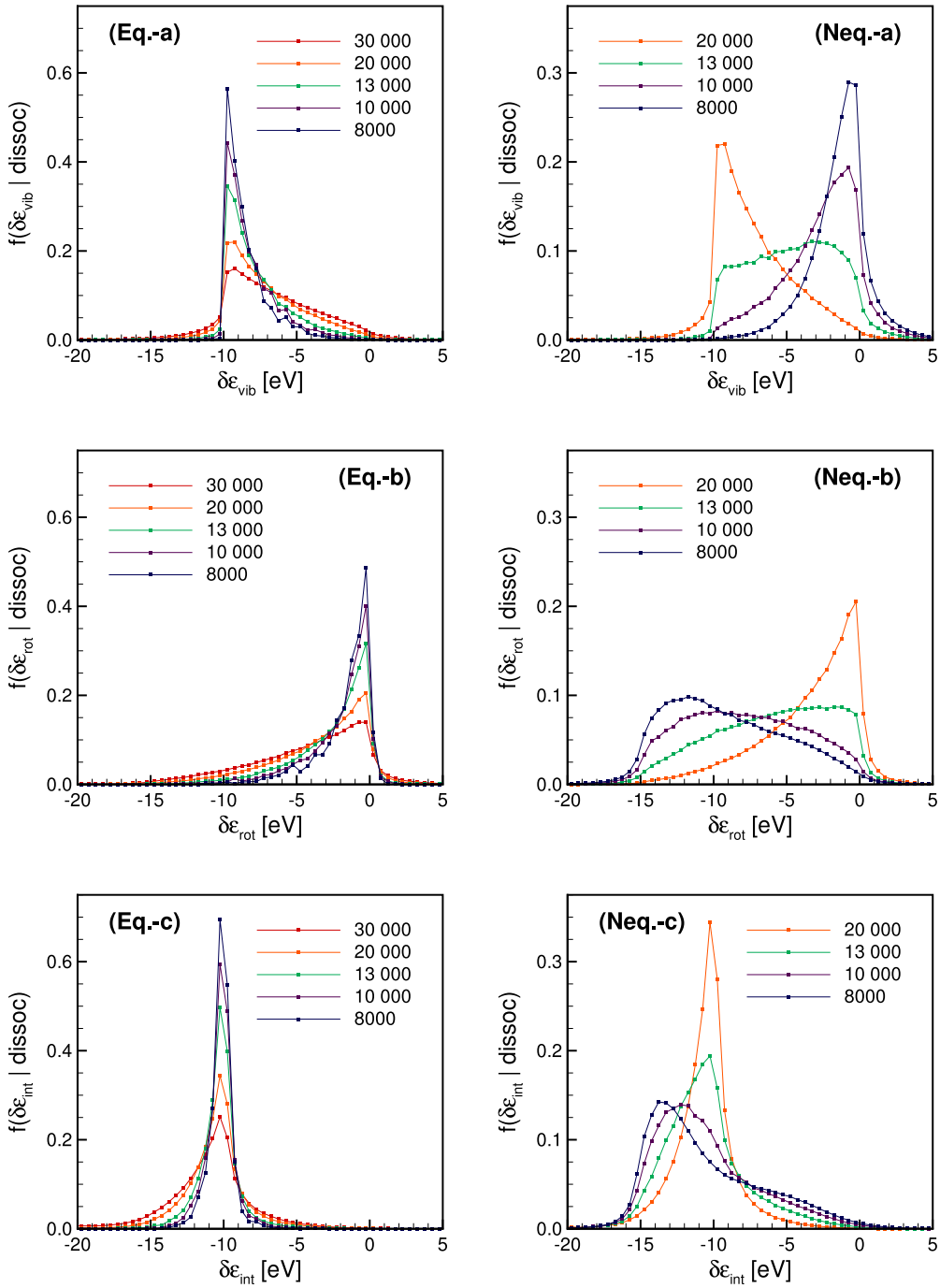

FIG. 11. PDFs of the changes in the vibrational internal energy $\delta\varepsilon_{\text{vib}}$, rotational internal energy $\delta\varepsilon_{\text{rot}}$, and total internal energy $\delta\varepsilon_{\text{int}}$ from the reactants to the products, for all *dissoc* trajectories. (Eq.) denotes results from five equilibrium runs; the legend in these plots indicates the temperature $T = T_{\text{v}}$. (Neq.) denotes results from four nonequilibrium runs; the legend in these gives the vibrational temperature T_{v} while the translational temperature T is held fixed at 20 000 K. Note the difference in scales of the vertical axes of the (Eq.) and (Neq.) plots. Temperatures are in K.

It is instructive to compare the last column of Table XIV with the last column of Table XI. At low temperatures, the magnitude of the average internal energy loss $\lfloor\delta\varepsilon_{\text{int}}\rfloor$ (among all dissociative collisions) is approximately equal to the average internal energy $\lfloor\varepsilon_{\text{int},1}\rfloor$ of $N_2^{(1)}$ (among *simple-dissoc* collisions in which that molecule dissociates). From Table VII, we know that dissociation at these conditions occurs almost entirely via *simple-dissoc* events. Together, these observations support the claim that dissociation occurs primarily from translational energy transfer at low-temperature thermal equilibrium. Indeed, in a *simple-dissoc* trajectory with only translational energy transfer, the internal energy of the dissociating molecule's collision partner remains unchanged; thus, the magnitude of total internal energy loss is exactly equal to the initial internal energy of the dissociating molecule. Using the language of Sec. V B 2, we say that dissociation is primarily induced via elastic-partner collisions rather than inelastic-partner collisions.

As the equilibrium temperature increases, the magnitude of $\lfloor\delta\varepsilon_{\text{int}}\rfloor$ increases slightly above $\lfloor\varepsilon_{\text{int},1}\rfloor$, perhaps reflecting

TABLE XIV. Statistics on initial properties of both reactant molecules and on the total change of energy from the reactants to the products. Three energy quantities are considered: the vibrational energy ε_{vib}, the rotational energy ε_{rot}, and the internal energy ε_{int}. The six columns $\bar{\varepsilon}_{\text{vib}}, \ldots, \lfloor\varepsilon_{\text{int}}\rfloor$ give properties for the total energy of the reactants, i.e., the sum of the initial energies of the two reactant molecules. An overbar indicates an average over the entire ensemble of trajectories. Half-brackets $\lfloor\cdot\rfloor$ indicate an average over only those trajectories that result in a *dissoc* event, i.e, $\lfloor x\rfloor$ means an average over the probability density function $f(x\,|\,\textit{dissoc})$. Finally, the δ symbols in the three columns $\lfloor\varepsilon_{\text{vib}}\rfloor, \ldots, \lfloor\varepsilon_{\text{int}}\rfloor$ indicate a difference from the reactants to the products, per Eq. (26). Data are from five equilibrium runs with $T = T_{\text{v}}$. Temperatures are in K and energies are in eV. See Figure 11(Eq.) for comparison.

$T = T_{\text{v}}$	$\bar{\varepsilon}_{\text{vib}}$	$\bar{\varepsilon}_{\text{rot}}$	$\bar{\varepsilon}_{\text{int}}$	$\lfloor\varepsilon_{\text{vib}}\rfloor$	$\lfloor\varepsilon_{\text{rot}}\rfloor$	$\lfloor\varepsilon_{\text{int}}\rfloor$	$\lfloor\delta\varepsilon_{\text{vib}}\rfloor$	$\lfloor\delta\varepsilon_{\text{rot}}\rfloor$	$\lfloor\delta\varepsilon_{\text{int}}\rfloor$
30 000	5.55	4.92	10.5	9.20	6.41	15.6	−6.78	−4.22	−11.0
20 000	4.01	3.51	7.52	9.09	5.09	14.2	−7.17	−3.42	−10.6
13 000	2.52	2.28	4.80	9.03	3.68	12.7	−7.76	−2.56	−10.3
10 000	1.89	1.74	3.62	9.13	2.91	12.0	−8.16	−2.05	−10.2
8 000	1.49	1.38	2.86	9.22	2.33	11.6	−8.49	−1.69	−10.2

the increasingly important role of *single-dissoc-swap* and *double-dissoc* events in the dissociation process, as documented in Table VII. Also notice that as $T = T_{\text{v}}$ increases, rotational energy loss accounts for a larger fraction of the total internal energy loss. This is consistent with the results in Table XI and Figure 9(Eq.), where we observed that low-v and high-j states play a more significant role in *simple-dissoc* trajectories as the equilibrium temperature increases. It is interesting to observe, however, that the average combined vibrational energy of the reactants in a dissociating trajectory is between 9.0 and 9.2 eV in all cases, as shown in the fifth column of Table XIV.

Figure 11(Neq.) and Table XV summarize results from the nonequilibrium test set. Comparing these data with the equilibrium results, we first notice that the shape of the PDF of $\delta\varepsilon_{\text{vib}}$ changes significantly as T_{v} decreases with T fixed. Indeed, the high likelihood of a large vibrational energy loss disappears, and the peak of the PDF moves towards zero. In fact, in the T = 20 000 K and T_{v} = 8000 K case, the most likely occurrence is a vibrational energy loss of about 0–1 eV. Conversely, the magnitude of the loss of rotational energy $\delta\varepsilon_{\text{rot}}$ increases as T_{v} decreases. The PDFs in Figure 11(Neq.-b) broaden, with their peaks moving toward more negative energy values. Accordingly, from Table XV, the average value of $\delta\varepsilon_{\text{vib}}$ decreases in magnitude, and the average value of $\delta\varepsilon_{\text{rot}}$ increases in magnitude. The PDFs of $\delta\varepsilon_{\text{int}}$ in Figure 11(Neq.-c) also broaden, with their peaks moving toward more negative values, though the average of $\delta\varepsilon_{\text{int}}$ over the dissociating trajectories remains approximately constant, ranging from −10.5 to −10.6 eV.

These observations are broadly consistent with our discussion in Sec. V C. From the sixth column of Table XV, we see that highly rotationally excited molecules play a more significant role in the dissociation process as the vibrational temperatures fall below the translational-rotational temperature. Also, again using the language of Sec. V B 2, we see further evidence of the importance of inelastic-partner collisions in promoting dissociation in these nonequilibrium cases. Consider the eighth column of Table XV and the ninth column of Table XII. In the nonequilibrium cases, the magnitude of the average vibrational energy loss $\lfloor\delta\varepsilon_{\text{vib}}\rfloor$ (among all dissociative collisions) is always slightly less than the average vibrational energy $\lfloor\varepsilon_{\text{vib},1}\rfloor$ of $N_2^{(1)}$ (among *simple-dissoc* collisions in which that molecule dissociates). This was never the case for the equilibrium cases, and it suggests the presence of dissociative trajectories with a product molecule of higher vibrational energy than either of the reactants. This, in turn, suggests the increasingly important role of internal energy exchange in these trajectories.

F. Future work

Further research in various areas would be useful. For example, we might re-run some tests in this paper with a PES constructed using the second-generation local interpolating moving least squares (L-IMLS-G2) fitting method, developed and applied to N_2 in earlier work.[85] It has been shown to be even more accurate than the fitting method described in Sec. II, but it is significantly more computationally expensive.

We anticipate that the results presented here will enable better modeling of the energy distributions in hypersonic flows and how they are coupled with the dissociation process. The reactant ensemble energy distributions that we discussed in this paper were clearly idealized and are intended to serve as

TABLE XV. Statistics on initial properties of both reactant molecules and on the total change of energy from the reactants to the products. The same conventions used in Table XIV are used here. Data are from four runs with T fixed at 20 000 K, and with T_{v} varied. See Figure 11(Neq.) for comparison.

T_{v}	$\bar{\varepsilon}_{\text{vib}}$	$\bar{\varepsilon}_{\text{rot}}$	$\bar{\varepsilon}_{\text{int}}$	$\lfloor\varepsilon_{\text{vib}}\rfloor$	$\lfloor\varepsilon_{\text{rot}}\rfloor$	$\lfloor\varepsilon_{\text{int}}\rfloor$	$\lfloor\delta\varepsilon_{\text{vib}}\rfloor$	$\lfloor\delta\varepsilon_{\text{rot}}\rfloor$	$\lfloor\delta\varepsilon_{\text{int}}\rfloor$
20 000	4.01	3.51	7.52	9.09	5.09	14.2	−7.17	−3.42	−10.6
13 000	2.51	3.57	6.07	5.98	7.64	13.6	−4.60	−5.97	−10.6
10 000	1.89	3.57	5.46	3.84	9.58	13.4	−2.64	−7.92	−10.6
8 000	1.49	3.58	5.06	2.52	10.8	13.3	−1.42	−9.11	−10.5

a guide to studying more realistic distributions. For example, there is no reason to believe *a priori* that a real gas undergoing vibrational relaxation will do so by moving through a series of Boltzmann distributions of vibrational energies. Research studying the actual time evolution of energy distributions in a dissociating gas is underway using particle-based simulation tools (originally developed for studying rarefied gas flows).[51] Actual distributions can also be studied by master equation simulations.[23–26,86]

VI. CONCLUSIONS

In this paper, we discussed a QCT analysis of $N_2 + N_2$ dissociative collisions under both thermal equilibrium and nonequilibrium conditions. An improved PES was constructed by a fit to electronic structure calculations for the N_4 system. The improvements consisted of additional quantum mechanical electronic structure calculations and an improved functional form of the fitting function that better models long-range interactions. Trajectories were prepared based on quantized rovibrational states of a N_2 molecule and on a two-temperature model that assumes one temperature applies to the vibrational manifold and another to the translational-rotational manifold. In all cases, we assumed approximately Boltzmann distributions of states for each energy mode and equilibrium between the translational and rotational modes. A stratified sampling strategy based on the impact parameter was used to accelerate convergence of the Monte Carlo integrations. We computed a total of over 2.4×10^9 trajectories over a range of translational-rotational and vibrational temperatures. We reported ensemble-averaged dissociation rate constants for 25 temperature combinations. Then, restricting our attention to a set of five equilibrium runs and a set of four nonequilibrium runs, we analyzed what subsets of trajectories contributed to the dissociation rate constants. For those equilibrium and nonequilibrium test sets, we examined PDFs of various quantities that characterize, in dissociating trajectories, the initial internal energies of reactant molecules and the changes in those energies.

Several important conclusions emerged. First, we saw that the influence of the translational-rotational temperature T on the dissociation rate constant is stronger when the vibrational temperature T_v is low, and vice versa. The Park two-temperature model[43,44] predicts rate constants that are smaller than our QCT results in almost all cases. Agreement is best when both T and T_v are low, and it is worst when either $T \ll T_v$ or $T_v \ll T$.

In studying contributions to the rate constants from various trajectory subsets, we noted that the contribution of low-impact-parameter collisions to the rate constant increases in two different scenarios: as the equilibrium temperature increases, or as T_v decreases while T is fixed. At higher temperatures, "swap" dissociation processes become more and more significant; they contributed over 28% to the rate constant in the 30 000 K equilibrium case. Even "double" dissociation events were not completely negligible at the highest temperatures. Across all cases we considered, quasibound states of N_2 played a crucial role in the dissociation process, with typical contributions of over 58% from trajectories with at least one quasibound reactant.

For equilibrium ensembles, we saw in Figures 9 and 11 that high-v and moderately-low-j molecules are predominant in the sets of dissociating trajectories, and this dominance becomes stronger as the temperature decreases. Dissociating trajectories tend to result in a vibrational energy loss from the reactants of up to about 10 eV and in a smaller rotational energy loss. (For comparison, the equilibrium dissociation energy of the diatomic potential we used is 9.917 eV.) As the temperature decreases, the average vibrational energy loss in a dissociating trajectory becomes larger in magnitude and less variable (i.e., the corresponding PDF is more sharply peaked), and the average rotational energy loss becomes smaller in magnitude and less variable. The average total internal energy loss is consistent at between −10.2 and −11.0 eV, and it again is less variable at lower temperatures. Broadly, we can conclude from these results that at equilibrium, vibrational energy plays a more important role in dissociation than does rotational energy in the sense that (1) there tends to be more vibrational energy than rotational energy in the reactants of dissociating trajectories, and (2) the change in vibrational energy from the reactants to the products in dissociating trajectories is typically larger than the change in rotational energy. Both biases become stronger as $T = T_v$ decreases. Also, we found that dissociation is induced primarily via translational energy transfer in *elastic-partner collisions*.

For nonequilibrium ensembles, we analyzed a representative set of four runs with $T_v \leq T$ and T fixed. As the vibrational temperature decreases below the translational-rotational temperature in these cases, the proportion of high-j and low-v molecules in the dissociating trajectories increases. In fact, we observed that when $T_v \ll T$, the PDF of the initial vibrational quantum number v_1 on the set of dissociating trajectories resembles a Boltzmann distribution, indicating a weak dependence of dissociation probability on the vibrational level. As T_v decreases while T is held constant, the magnitude of the average rotational energy loss from the reactants to the products in dissociating trajectories increases, while the magnitude of the average vibrational energy loss decreases. We can summarize these behaviors by concluding that rotational energy plays an increasingly important energy-providing role in promoting dissociation when there is a decline of average vibrational energy in the gas. Even in these nonequilibrium cases, the average total internal energy loss from the reactants to the products remains at between −10.5 and −10.6, values similar to those from the equilibrium cases. *Inelastic-partner collisions* are more significant in these nonequilibrium cases than in the equilibrium cases, but translational energy transfer remains the dominant mechanism of dissociation.

ACKNOWLEDGMENTS

J. D. Bender was supported in this work by the U.S. Department of Energy Computational Science Graduate Fellowship (DOE CSGF) under Grant No. DE-FG02-97ER25308. Other work was supported by the U.S. Air Force Office of Scientific Research (AFOSR) under the Multidisciplinary Uni-

versity Research Initiative (MURI) Grant Nos. FA9550-10-1-0563 and FA9550-12-1-0064 and by the Department of Defense National Security Science and Engineering Faculty Fellowship. The views and conclusions contained herein are those of the authors and should not be interpreted as representing the official policies or endorsements, either expressed or implied, of the University of Minnesota, DOE, AFOSR, DOD, or the U.S. Government.

[1]Y. Paukku, K. R. Yang, Z. Varga, and D. G. Truhlar, J. Chem. Phys. **139**, 044309 (2013); Erratum, **140**, 019903 (2014).
[2]J. D. Bender, I. Nompelis, P. Valentini, S. Doraiswamy, T. Schwartzentruber, G. V. Candler, Y. Paukku, K. R. Yang, Z. Varga, and D. G. Truhlar, AIAA Paper 2014-2964, 2014.
[3]H. Johnston and J. Birks, Acc. Chem. Res. **5**, 327 (1972).
[4]B. J. McCoy and R. G. Carbonell, J. Chem. Phys. **66**, 4564 (1977).
[5]H. Teitelbaum, Chem. Phys. **124**, 55 (1988).
[6]J. E. Dove and D. G. Jones, J. Chem. Phys. **55**, 1531 (1971).
[7]J. E. Dove and D. G. Jones, Chem. Phys. Lett. **17**, 134 (1972).
[8]P. Hammerling, J. D. Teare, and B. Kivel, Phys. Fluids **2**, 422 (1959).
[9]C. E. Treanor and P. V. Marrone, Phys. Fluids **5**, 1022 (1962).
[10]P. V. Marrone and C. E. Treanor, Phys. Fluids **6**, 1215 (1963).
[11]W. G. Valance, J. Phys. Chem. **85**, 1305 (1981).
[12]V. H. Shu, J. P. Appleton, and J. C. Keck, J. Chem. Phys. **53**, 2547 (1970).
[13]J. H. Kiefer, H. P. G. Joosten, and W. D. Breshears, Chem. Phys. Lett. **30**, 424 (1975).
[14]I. V. Adamovich, S. O. Macheret, J. W. Rich, and C. E. Treanor, AIAA J. **33**, 1064 (1995).
[15]I. V. Adamovich, S. O. Macheret, J. W. Rich, and C. E. Treanor, AIAA J. **33**, 1070 (1995).
[16]I. V. Adamovich and J. W. Rich, J. Chem. Phys. **109**, 7711 (1998).
[17]S. O. Macheret and I. V. Adamovich, J. Chem. Phys. **113**, 7351 (2000).
[18]D. A. Gonzales and P. L. Varghese, J. Thermophys. Heat Transfer **8**, 236 (1994).
[19]D. A. Gonzales and P. L. Varghese, Chem. Phys. **195**, 83 (1995).
[20]D. A. Gonzales, Int. J. Chem. Kinet. **29**, 791 (1997).
[21]S. O. Macheret and J. W. Rich, Chem. Phys. **174**, 25 (1993).
[22]D. G. Truhlar and N. C. Blais, J. Am. Chem. Soc. **99**, 8108 (1977).
[23]D. G. Truhlar, N. C. Blais, J.-C. J. Hajduk, and J. H. Kiefer, Chem. Phys. Lett. **63**, 337 (1979).
[24]J. E. Dove and S. Raynor, J. Phys. Chem. **83**, 127 (1979).
[25]K. Haug, D. G. Truhlar, and N. C. Blais, J. Chem. Phys. **86**, 2697 (1987); Erratum, **96**, 5556 (1992).
[26]S. P. Sharma and D. W. Schwenke, J. Thermophys. Heat Transfer **5**, 469 (1991).
[27]P. G. Martin, D. H. Schwarz, and M. E. Mandy, Astrophys. J. **461**, 265 (1996).
[28]J. G. Kim, O. J. Kwon, and C. Park, J. Thermophys. Heat Transfer **23**, 443 (2009).
[29]J. G. Kim, O. J. Kwon, and C. Park, J. Thermophys. Heat Transfer **24**, 281 (2010).
[30]M. Capitelli, G. Colonna, and F. Esposito, J. Phys. Chem. A **108**, 8930 (2004).
[31]F. Esposito, I. Armenise, and M. Capitelli, Chem. Phys. **331**, 1 (2006).
[32]R. Jaffe, D. Schwenke, and G. Chaban, AIAA Paper 2010-4517, 2010.
[33]M. Panesi, R. L. Jaffe, D. W. Schwenke, and T. E. Magin, J. Chem. Phys. **138**, 044312 (2013).
[34]M. Panesi, A. Munafò, T. E. Magin, and R. L. Jaffe, Phys. Rev. E **90**, 013009 (2014).
[35]N. Parsons, D. A. Levin, A. C. T. van Duin, and T. Zho, J. Chem. Phys. **141**, 234307 (2014).
[36]M. Karplus, R. N. Porter, and R. D. Sharma, J. Chem. Phys. **43**, 3259 (1965).
[37]D. G. Truhlar and J. T. Muckerman, in *Atom-Molecule Collision Theory: A Guide for the Experimentalist*, edited by R. B. Bernstein (Plenum Press, New York, 1979), pp. 505–566.
[38]W. G. Vincenti and C. H. Kruger, *Introduction to Physical Gas Dynamics* (Krieger Publishing Company, Malabar, FL, 2002), Chaps. II and IV.
[39]R. C. Millikan and D. R. White, J. Chem. Phys. **39**, 3209 (1963).
[40]I. Oppenheim, J. Geophys. Res. **68**, 5947, doi:10.1029/JZ068i021p05947 (1963).
[41]R. S. Berry, S. A. Rice, and J. Ross, *Physical Chemistry* (Wiley, New York, 1980), p. 1077.
[42]C. Park, J. Thermophys. Heat Transfer **3**, 233 (1989).
[43]C. Park, *Nonequilibrium Hypersonic Aerothermodynamics* (Wiley, New York, 1990), p. 326.
[44]C. Park, J. Thermophys. Heat Transfer **7**, 385 (1993).
[45]C. F. Hansen, AIAA J. **31**, 2047 (1993).
[46]L. B. Ibragimova, G. D. Smekhov, and O. P. Shatalov, Fluid Dyn. **34**, 153 (1999).
[47]C. Park, R. L. Jaffe, and H. Patridge, J. Thermophys. Heat Transfer **15**, 76 (2001).
[48]M. Lino da Silva, V. Guerra, and J. Loureiro, Chem. Phys. **342**, 275 (2007).
[49]A. Munafò, M. Panesi, R. L. Jaffe, G. Colonna, A. Bourdon, and T. E. Magin, Eur. Phys. J. D **66**, 188 (2012).
[50]P. Valentini, C. Zhang, and T. E. Schwartzentruber, Phys. Fluids **24**, 106101 (2012).
[51]P. Norman, P. Valentini, and T. Schwartzentruber, J. Comput. Phys. **247**, 153 (2013).
[52]F. Lordet, J. G. Méolans, A. Chauvin, and R. Brun, Shock Waves **4**, 299 (1995).
[53]M. Capitelli, I. Armenise, and C. Gorse, J. Thermophys. Heat Transfer **11**, 570 (1997).
[54]B. J. Braams and J. M. Bowman, Int. Rev. Phys. Chem. **28**, 577 (2009).
[55]Z. Xie and J. M. Bowman, J. Chem. Theory Comput. **6**, 26 (2010).
[56]K. Andersson, P.-Å. Malmqvist, and B. O. Roos, J. Chem. Phys. **96**, 1218 (1992).
[57]H.-J. Werner, Mol. Phys. **89**, 645 (1996).
[58]E. Papajak, H. R. Leverentz, J. Zheng, and D. G. Truhlar, J. Chem. Theory Comput. **5**, 1197 (2009).
[59]See supplementary material at http://dx.doi.org/10.1063/1.4927571 for the additional electronic structure data.
[60]G. Herzberg, in *Molecular Spectra and Molecular Structure*, Spectra of Diatomic Molecules Vol. I, 2nd ed. (D. Van Nostrand, Princeton, 1950).
[61]E. Garcia, T. Martínez, and A. Laganà, Chem. Phys. Lett. **620**, 103 (2015).
[62]R. J. Duchovic, Y. L. Volobuev, G. C. Lynch, D. G. Truhlar, T. C. Allison, A. F. Wagner, B. C. Garret, and J. C. Corchado, Comput. Phys. Commun. **144**, 169 (2002); Erratum, **156**, 319 (2004), POTLIB is freely available online at http://comp.chem.umn.edu/potlib.
[63]C. Petrongolo, J. Mol. Struct. **175**, 215 (1988).
[64]J. N. Murrell, O. Novaro, S. Castillo, and V. Saunders, Chem. Phys. Lett. **90**, 421 (1982).
[65]I. S. K. Kerkines, Z. Wang, P. Zhang, and K. Morokuma, Mol. Phys. **107**, 1017 (2009).
[66]M. M. Francl and J. P. Chesick, J. Phys. Chem. **94**, 526 (1990).
[67]T. J. Lee and J. E. Rice, J. Chem. Phys. **94**, 1215 (1991).
[68]M. L. Leininger, T. J. Van Huis, and H. F. Schaefer III, J. Phys. Chem. A **101**, 4460 (1997).
[69]J. I. Steinfeld, J. S. Francisco, and W. L. Hase, *Chemical Kinetics and Dynamics*, 2nd ed. (Prentice Hall, Upper Saddle River, NJ, 1999), Chaps. 1, 6, and 8.
[70]R. D. Levine, *Molecular Reaction Dynamics* (Cambridge University Press, Cambridge, 2005), Chap. 3.
[71]D. J. Griffiths, *Introduction to Quantum Mechanics*, 2nd ed. (Pearson Prentice Hall, Upper Saddle River, NJ, 2005).
[72]C. M. Bender and S. A. Orszag, *Advanced Mathematical Methods for Scientists and Engineers: Asymptotic Methods and Perturbation Theory* (Springer-Verlag, New York, 1999), Chap. 10.
[73]M. Galassi *et al.*, *GNU Scientific Library Reference Manual*, 3rd ed. (Network Theory Ltd., 2013), http://www.gnu.org/software/gsl/.
[74]W. H. Press, S. A. Teukolsky, W. T. Vetterling, and B. P. Flannery, *Numerical Recipes in FORTRAN: The Art of Scientific Computing*, 2nd ed. (Cambridge University Press, Cambridge, 1992), Chaps. 9 and 10.
[75]K. F. Riley, M. P. Hobson, and S. J. Bence, *Mathematical Methods for Physics and Engineering*, 3rd ed. (Cambridge University Press, Cambridge, 2013), Chap. 27.
[76]D. A. McQuarrie, *Statistical Mechanics* (University Science Books, Mill Valley, CA, 2000), Chaps. 2 and 6.
[77]D. L. Bunker, in *Methods in Computational Physics, Advances in Research and Applications*, Atomic and Molecular Scattering Vol. 10, edited by B. Alder, S. Fernbach, and M. Rotenberg (Academic Press, New York, 1971), p. 287.

[78]D. Frenkel and B. Smit, *Understanding Molecular Simulation: From Algorithms to Applications* (Academic Press, San Diego, 2002).
[79]The HDF Group, Hierarchical Data Format, version 5, 1997-2014, http://www.hdfgroup.org/HDF5/.
[80]M. Mascagni and A. Srinivasan, ACM Trans. Math. Software **26**, 436 (2000), the SPRNG library is available at http://www.sprng.org/ (accessed 27 January 2015). We used version 2.0 of the library in this work.
[81]S. Byron, J. Chem. Phys. **44**, 1378 (1966).
[82]J. P. Appleton, M. Steinberg, and D. J. Liquornik, J. Chem. Phys. **48**, 599 (1968); Erratum, **49**, 2468 (1968).
[83]R. K. Hanson and D. Baganoff, AIAA J. **10**, 211 (1972).
[84]MATLAB and Optimization Toolbox Release 2013a, The MathWorks, Inc., Natick, Massachusetts, 2013.
[85]J. D. Bender, S. Doraiswamy, D. G. Truhlar, and G. V. Candler, J. Chem. Phys. **140**, 054302 (2014).
[86]K. Haug and D. G. Truhlar, J. Phys. Chem. **89**, 3198 (1985).